

MASTER'S THESIS
MASTER'S DEGREE IN QUANTUM SCIENCE AND TECHNOLOGY

**ATOMIC PROPERTIES & RED LASER SYSTEM
FOR A SR-BASED RYDBERG QUANTUM SIMULATOR**

DERIK ROCHLITZER PUIG

Supervised by
Quentin Redon
Leticia Tarruell

ICFO^R

 **Master in Quantum
Science and Technology
Barcelona**

Barcelona, July 2025

Atomic Properties & Red Laser System for a Sr-Based Rydberg Quantum Simulator

Derik Rochlitzer Puig

Supervised by: Quentin Redon and Leticia Tarruell

ICFO, Mediterranean Technology Park, Avinguda Carl Friedrich Gauss, 3, 08860 Castelldefels, Barcelona
6 July 2025

Quantum simulation seeks to study physical models that are beyond the reach of classical computation. Within this scope, ICFO's Ultracold Quantum Gases group is developing a strontium Rydberg atom array platform to simulate high-dimensional lattice gauge theories with plaquette interactions, many-body couplings yet to be experimentally realised. This experiment requires a detailed theoretical understanding and a technically involved setup.

This master's thesis contributes to both fronts. On the theoretical side, we studied strontium's clock state and its magnetic-field-induced excitation, characterised the properties and interactions of Rydberg states, and analysed a scheme for selective Rydberg excitation based on light shifts. Our results show that the clock transition can be broadened to the 0.1 mHz range to enable excitation, that Rydberg states with $n \approx 60$ offer favourable interaction landscapes and coupling strengths, and that selective excitation should be feasible by scaling the intensity of optical tweezers.

Experimentally, we implemented the core of the 689 nm laser system, including a slave diode for power amplification and an optical cavity for monitoring. We also verified the finesse of an ultrastable cavity for future frequency stabilisation and successfully tested the Pound-Drever-Hall locking technique on the monitoring cavity.

Overall, these developments mark significant progress towards completing the experimental platform and provide a theoretical basis for future design choices. The future steps will focus on assembling the remaining experimental systems and testing our theoretical predictions.

Keywords: Quantum simulation, cold atoms, strontium, clock transition, Rydberg atoms, Rydberg-Rydberg interactions, red laser system, slave laser diode, ultrastable optical cavity, Pound-Drever-Hall locking.

Acknowledgements

The present master's thesis, even if under my name, is the result of a collective effort. Thus, I would like to write a few words to thank those who have supported me along the way. First of all, I want to express my gratitude to Leticia (and Alessio for his part) for granting me the opportunity to try experimental physics in ICFO's Ultracold Quantum Gases group. As a novice experimentalist, all the work I have carried out and all the experience I have acquired would not have been possible without the guidance of Quentin. I am truly grateful for the numerous hours that you have invested in teaching, supervising and discussing with me. This master's thesis would not be what it is without your support. And since I am talking about supervisors, I cannot forget about Julia. I also have to thank you for all the hours that I stole from you, your guidance through the theory proposal and, of course, your invaluable moral support. It is a shame that future students will lose such a supervisor...

I also want to thank the rest of the huge Rydberg group: Ana and Roxana. It has been a pleasure to share the office and the lab with you over the last few months. Thank you for being there when any questions or dumb doubts arose along the way.

Moreover, I am sincerely grateful to the entire QGE team for being welcoming and being there, always willing to lend their time to help when necessary.

Finalment, vull agrair a totes les persones properes que m'han acompanyat i fet costat fins ara. A l'Ana, per ser la meva companya de viatge i ajudar-me a continuar endavant quan les forces no acompanyen. Als amics propers, per ser la vàlvula d'escapament amb qui tot flueix. I, òbviament, als meus pares, per ser el suport incondicional de la meva vida, oferint tot i més sense esperar res a canvi.

Contents

List of Figures	IV
List of Abbreviations	V
Introduction	1
1 Background	2
1.1 A Taste of Rydberg Physics and Lattice Gauge Theories	2
1.2 Simulating Two-Dimensional Gauge Theories with Rydberg Atom Arrays .	3
1.3 Why Strontium?	5
2 Atomic Properties and Interactions	6
2.1 Magnetic Response of the Clock State	6
2.2 Characterisation of Rydberg states	8
2.2.1 Lifetimes and Rabi Frequencies	8
2.2.2 Rydberg-Rydberg Interactions	9
2.3 Light Shifts and Selective Rydberg Excitation	11
2.4 Conclusions and Outlook	12
3 The Red Laser System	12
3.1 Overview of the Experiment	12
3.1.1 Polarisation Fluctuations in the 689 nm Laser	13
3.1.2 Frequency Tuning with Acousto-Optic Modulators	14
3.2 Power Amplification with a Slave Diode	14
3.2.1 Setup	14
3.2.2 Monitoring with an Optical Cavity	15
3.3 Frequency Stabilisation with an Ultrastable Cavity	16
3.3.1 Characterisation of the Ultrastable Cavity	17
3.3.2 Pound-Drever-Hall Technique for Frequency Stabilisation	18
3.4 Conclusions and Outlook	20
4 Conclusions	20
Bibliography	21
Annexes	
A Numerical Analysis of the Clock State’s Magnetic Response	25
A.1 Building and Diagonalising the Zeeman Hamiltonian	25
A.2 Calculating the Linewidth and the Rabi Frequency	26
B Studying Rydberg-Rydberg Interactions with pairinteraction	27
C Computing Atomic Polarisabilities	28
C.1 Atomic Polarisabilities of Rydberg States	29
D Reflection Signal of an Optical Cavity when Scanning the Frequency	29
E Pictures of the Experimental Setup	32

List of Figures

1	Diagrams on lattice gauge theories	3
2	Properties of $5s^2\ ^1S_0 \rightarrow 5s5p\ ^3P_0$ as a function of B	7
3	Properties of $5s5p\ ^3P_0 \rightarrow 5sns\ ^3S_1$ as a function of n	8
4	Properties of Rydberg-Rydberg interactions as a function of n	10
5	Light shifts of the clock and Rydberg state	11
6	Schematic of the setup for the main optical paths	13
7	Schematics of the setup for the slave diode and intensity profiles	15
8	Schematic of the setup for monitoring and the transmission spectrum	16
9	Schematic of the setup for cavity characterisation and the reflection signal	18
10	Schematic of the modified setup for monitoring and the PDH error signal	19

List of Abbreviations

- › **AOM**: Acousto-optic modulator
- › **CG**: Clebsch-Gordan
- › **EOM**: Electro-optic modulator
- › **FWHM**: Full width at half maximum
- › **FSR**: Free spectral range
- › **MOT**: Magneto-optical trap
- › **PBS**: Polarising beamsplitter
- › **PDH**: Pound-Drever-Hall
- › **PT**: Perturbation theory
- › **RK**: Rokhsar-Kivelson
- › **Ry**: Rydberg
- › **WP**: Waveplate

Introduction

Understanding the fundamental nature of the universe has always been the central aim of physics. To this end, increasingly sophisticated computational techniques have been designed. Yet, simulating quantum many-body systems, particularly those involving strong interactions, remains an outstanding challenge for classical computing. Nearly half a century after Feynman’s seminal proposal to simulate quantum mechanics using quantum systems [1], quantum simulation has undergone remarkable progress. Today, experimental developments are enabling quantum simulators to probe physical regimes previously considered inaccessible.

Quantum simulation comprises two schemes: digital and analogue. At present, each relies on specialised platforms tailored to specific problems, remaining distant from achieving a universal, all-purpose quantum simulator. The digital approach mirrors conventional computation, using qubits and sequences of quantum logic gates to reproduce the time evolution of a system. In contrast, analogue quantum simulation engineers a controllable physical system to mimic the behaviour of another. By mapping the dynamics of a target system onto a more accessible quantum platform, one can explore the microscopic origin of complex quantum phenomena under well-controlled conditions [2].

A variety of experimental platforms have been developed for this purpose, including trapped ions [3], superconducting qubits [4], photonic circuits [5], quantum dots [6], ultracold molecules [7], and ultracold neutral atoms [8–10]. Each system offers particular advantages, making them well-suited for specific purposes. In this work, we focus on ultracold neutral atoms, excelling in their scalability, long coherence times, and capability of simulating strongly interacting systems with single-atom addressability and control.

ICFO’s Ultracold Quantum Gases group utilises ultracold atomic systems to explore fundamental phenomena in quantum many-body systems and push the frontiers of condensed matter physics. These efforts aim to provide insight into phenomena that are not yet fully understood, such as superconductivity and exotic quantum phases, crucial to the development of novel materials for next-generation technologies.

In this context, we are building a new experiment based on optical tweezer arrays [11, 12] of strontium atoms excited to Rydberg states (see [Section 1.1](#)). The extensive tunability in Rydberg-based systems provides access to a broad range of physical regimes, making them ideal for probing diverse quantum models. Our platform will realise programmable spin models, which implement gauge theories emerging from low-energy effective descriptions of condensed matter systems (see also [Section 1.1](#)). In particular, one of the primary objectives is to experimentally validate a novel proposal for simulating many-body interactions in 2D lattice gauge theories [13].

The present master’s thesis contributes to the development of this experiment along two complementary lines. First, we carried out a theoretical characterisation of the relevant atomic levels of strontium to ensure the fulfilment of requirements imposed by the experimental setup and the proposed model. Second, we implemented a narrow line red laser system, key for achieving temperatures on the order of μK within the experiment.

The structure of the manuscript is as follows. In [Section 1](#), we introduce the theoretical framework underlying Rydberg physics, the target spin model, and the motivations for selecting strontium as the atomic species. [Section 2](#) presents the characterisation of relevant atomic levels, such as the clock and Rydberg states, and implications for the experimental design. Finally, [Section 3](#) details the work carried out on the experimental setup, focusing on the development of the red laser system.

1 Background

Before presenting the results of this master's thesis, it is worthwhile to introduce key theoretical concepts on Rydberg atoms and lattice gauge theories. Furthermore, we will outline the physics targeted by the new experiment at ICFO and discuss the choice of strontium as the atomic species.

1.1 A Taste of Rydberg Physics and Lattice Gauge Theories

A Rydberg (Ry) atom is an atom with an electron excited to a Ry state, *i.e.*, an atomic level with a high principal quantum number, n . Ry states exhibit unique properties, such as large orbital radii, strong and tunable interactions, and long lifetimes [14]. This last feature allows us to treat Ry atoms as effective two-level systems. In the following, we focus on Ry interactions, given their relevance in later sections.

To study the electromagnetic interaction between two naturally neutral Ry atoms, we must employ a multipole expansion [15]. The first non-vanishing term is the dipole-dipole interaction given by

$$\hat{V}_{\text{dip}} = \frac{1}{4\pi\epsilon_0 R^3} \left[\hat{\mathbf{d}}_1 \cdot \hat{\mathbf{d}}_2 - 3(\mathbf{u} \cdot \hat{\mathbf{d}}_1)(\mathbf{u} \cdot \hat{\mathbf{d}}_2) \right], \quad (1)$$

where R is the separation between both atoms, \mathbf{u} is the unit vector joining them, and $\hat{\mathbf{d}}_i$ is the dipole operator of atom $i = \{1, 2\}$.

If the atoms are far, such that $d_1 \cdot d_2 / R^3 \ll 1$, we can treat the interaction perturbatively for the Ry-Ry pair state $|rr\rangle$. The first-order correction is zero, given that neutral atoms do not have a net dipole moment, $\langle r | \hat{\mathbf{d}} | r \rangle = 0$. The second-order correction is

$$\Delta E_{rr}^{(2)} = \sum_{r'r''} \frac{|\langle r'r'' | \hat{V}_{\text{dip}} | rr \rangle|^2}{E_{rr} - E_{r'r''}}, \quad (2)$$

where the sum runs over all possible electronic states. In practice, due to the denominator, the states that dominantly contribute are those close in energy to the $|rr\rangle$ state.

Merging eqs. (1) and (2), we write

$$\Delta E_{rr}^{(2)} = C_6 / R^6. \quad (3)$$

This expression is the well-known van der Waals interaction, commonly used to describe the interaction potential between atoms in Ry states. However, it arises from perturbation theory and is only valid when R is sufficiently large. At short distances, the correction from eq. (3) grows rapidly and quickly becomes comparable to $E_{rr} - E_{r'r''}$, invalidating the perturbative approach. In this limit, known as the Förster regime, the interaction potential varies as $1/R^3$, and the original $|rr\rangle$ state mixes with others close in energy. We will examine this breakdown and the resulting interaction landscape in Section 2.2.2.

Additionally, note that we could derive an equivalent result for atoms in their ground state. Yet, the C_6 coefficient would be significantly smaller. For Ry atoms, the dipole matrix element between different levels scales as n^2 , the energy as n^{-2} and the energy difference between neighbouring states as n^{-3} [14]. Consequently, the terms in eq. (2), and hence C_6 , scale as $(n^2 \cdot n^2)^2 / n^{-3} = n^{11}$, making them orders of magnitude larger for high- n Ry states than for the ground state.

These enhanced interactions lead to the Ry blockade, a central aspect of Ry physics. If a laser couples the ground state to a Ry state, the interaction shifts the energy of $|rr\rangle$ out of resonance. As a result, two nearby atoms cannot be simultaneously excited. This blockade

regime takes place when the interaction strength matches the laser coupling, $\hbar\Omega \approx C_6/R^6$, defining the blockade radius as $R_b = \sqrt[6]{C_6/\hbar\Omega}$, with Ω the transition's Rabi frequency (see inset in [Figure 1a](#)) [10].

The tunable, strong interactions of Ry atoms make them a promising platform for simulating spin models, particularly Ising-like ones [16–18]. In turn, these spin models map to numerous many-body descriptions, among which we focus on lattice gauge theories. These descriptions interest our group for their deep connections with condensed matter phenomena and high-energy physics. In short, gauge theories arise by promoting a global continuous symmetry to a local one, enforced independently at each point in space and time [19]. These theories, central to modern physics, underpin fundamental frameworks such as the Standard Model of particle physics [20]. In condensed matter systems, gauge theories can also emerge in low-energy descriptions, where local constraints and correlations give rise to effective gauge degrees of freedom. For example, such models are convenient for describing the fractional quantum Hall effect [21], high-temperature superconductivity [22] or quantum spin liquids [23].

Nonetheless, specific regimes of gauge theories remain inaccessible to classical approaches. An alternative is to discretise these theories, yielding lattice gauge theories that can be mapped onto quantum simulation platforms such as Ry atom arrays, where we can explore and control phenomena intrinsic to the original models. In these formulations, matter and charges are placed at the lattice sites, while field variables correspond to the links connecting them (see left of [Figure 1a](#)).

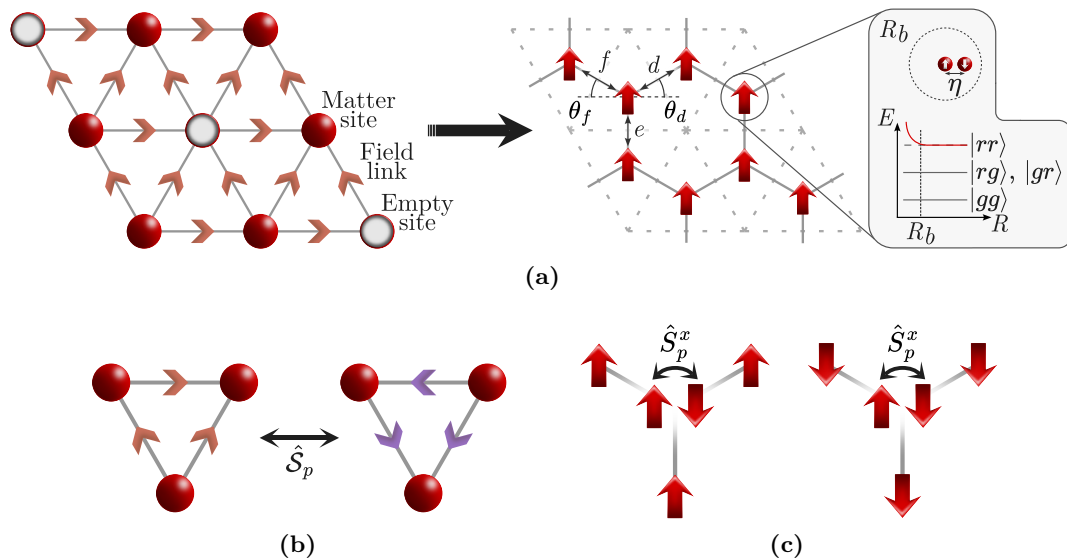


Figure 1: (a) The proposal by A. Celi *et al.* [13] maps a triangular lattice gauge theory to the dual hexagonal lattice, where each spin is an atom pair within the Ry blockade radius. (b) The \hat{S}_p operator in the original RK Hamiltonian flips all field spins in a plaquette. (c) On the dual lattice, plaquette interactions reduce to flipping only if all neighbouring spins are aligned.

1.2 Simulating Two-Dimensional Gauge Theories with Rydberg Atom Arrays

A main challenge in simulating lattice gauge theories beyond one spatial dimension is implementing plaquette interactions, which couple link variables around a closed loop (*e.g.*, [Figure 1b](#)). These interactions correspond to many-body processes that are non-trivial to engineer in quantum simulators. Nevertheless, they are central in many models, as in electromagnetism, where they encode magnetic interactions.

As a proof of principle, in the new experiment at ICFO, we aim to simulate the Rokhsar-Kivelson (RK) Hamiltonian, a spin-1/2 model initially proposed in the study of high-temperature conductivity, quantum dimers and resonating valence bond physics [24, 25]:

$$\hat{H}_{\text{RK}} = -J \sum_p \left[(\hat{S}_p + \hat{S}_p^\dagger) - \lambda (\hat{S}_p + \hat{S}_p^\dagger)^2 \right], \quad (4)$$

where the sum runs over all plaquettes, \hat{S}_p is an operator that flips all the plaquette's spins (Figure 1b), J sets the rate of such flipping, and λ modulates the potential-like term. Thus, plaquette interactions are intrinsic to the RK model. Successfully simulating eq. (4) would mark a significant step toward the experimental implementation of such interactions.

In the work by A. Celi *et al.* [13], they reformulate eq. (4) to implement it with a Ry atom array. The authors find a dual formulation where the plaquette's spins are mapped to spins-1/2 located at the dual sites (Figure 1a), such that the Hamiltonian becomes

$$\hat{H}_{\text{RK}}^* = -J \sum_p (\hat{P}_p^\uparrow + \hat{P}_p^\downarrow) (2\hat{S}_p^x - \lambda). \quad (5)$$

In this case, $\hat{P}_p^{\uparrow, \downarrow}$ are projectors onto states where all the spins around a site of the dual lattice, p , are in state $|\uparrow\rangle$ or $|\downarrow\rangle$, respectively. We call these configurations flippable plaquettes, given that \hat{S}_p^x , the usual spin-1/2 operator, can only flip spin p if the neighbouring ones are within the subspace spanned by $\hat{P}_p^\uparrow + \hat{P}_p^\downarrow$ (Figure 1c).

Moreover, eq. (5) evinces the role of the λ -term as a chemical potential, effectively counting the number of flippable plaquettes in the system. We can easily identify two distinct phases, which correctly map to the phase diagram of the original Hamiltonian (eq. (4)). When $\lambda \ll 0$, flippable plaquettes stabilise, and the system falls into a fully flippable ground state, where all dual spins are aligned. When $\lambda \gg 0$, flippable plaquettes are not favoured, and the system freezes into a configuration where no spin flips are possible.

This new formulation reduces the many-body interactions in eq. (4) to a spin flipping under a generalised blockade condition. This behaviour reminds us of the Ry blockade presented in Section 1.1. However, two configurations allow a spin-flip instead of a single one, in contrast to the standard blockade mechanism.

Because of such a generalised blockade condition, one needs to resort to sophisticated methods to simulate \hat{H}_{RK}^* with a Ry atom array. In the experiment at ICFO, we intend to implement a hexagonal array, which reproduces the dual formulation of the RK model on a triangular lattice, as shown by J. Bergmann [26]. Following the approach proposed by A. Celi *et al.*, two atoms occupy each site. These atoms are at a distance, η , smaller than the Ry blockade, so only one can be excited to the Ry state. Then, with a large negative detuning ($\Delta < 0$, $\Omega \ll |\Delta|$), the atomic pair behaves as a single spin, depending on which atom (left or right) is excited. From second-order perturbation theory, the effective Hamiltonian that governs the pair's dynamics is

$$\hat{H}_p \approx 2 \cdot \frac{2\Omega^2}{3|\Delta|} \cdot \hat{S}_p^x = -2J\hat{S}_p^x. \quad (6)$$

By including nearest-neighbour interactions between sites in a periodic lattice, the Hamiltonian of the system takes the form of an anisotropic Ising Hamiltonian:

$$\hat{H}_{\text{Ry}} = \sum_p \hat{H}_p + \hat{V}_p^{\text{NN}} = \sum_p -2J\hat{S}_p^x + \left[F(\mathbf{d}, \boldsymbol{\eta}) \hat{S}_{p+\mathbf{d}}^z + F(\mathbf{f}, \boldsymbol{\eta}) \hat{S}_{p+\mathbf{f}}^z + F(\mathbf{e}, \boldsymbol{\eta}) \hat{S}_{p-\mathbf{e}}^z \right] \hat{S}_p^z, \quad (7)$$

where $\mathbf{j} = \{\mathbf{d}, \mathbf{f}, \mathbf{e}\}$ are the vectors defining the geometry of the lattice (see [Figure 1a](#)), and $F(\mathbf{j}, \boldsymbol{\eta})$ sets the strength of the interactions:

$$F(\mathbf{j}, \boldsymbol{\eta}) = 2C_6|\boldsymbol{\eta}|^6 \left(\frac{2}{|\mathbf{j}|^6} - \frac{1}{|\mathbf{j} + \boldsymbol{\eta}|^6} - \frac{1}{|\mathbf{j} - \boldsymbol{\eta}|^6} \right). \quad (8)$$

Tuning the geometry of the lattice allows us to engineer energy offsets for different states through the second term in [eq. \(7\)](#), mimicking the action of the projectors $\hat{P}_p^{\uparrow, \downarrow}$. Particularly, by setting $F(\mathbf{d}, \boldsymbol{\eta}) = F(\mathbf{f}, \boldsymbol{\eta}) = -2F(\mathbf{e}, \boldsymbol{\eta})$, we achieve an offset only for states where the spins around p are not all $|\uparrow\rangle$ nor $|\downarrow\rangle$. If this energy shift is large, only the subspace spanned by $\hat{P}_p^{\uparrow} + \hat{P}_p^{\downarrow}$ will intervene in the dynamics, as in [eq. \(5\)](#). Also, one can verify that considering next-nearest-neighbours contributions yields the λ -term, hence mimicking the full RK Hamiltonian.

In summary, the proposals by A. Celi *et al.* and J. Bergmann [[13](#), [26](#)] offer a viable approach to simulating experimentally the RK model, as well as other Ising-like Hamiltonians with anisotropic interactions, achieved through a dual formulation encoded in the geometry of a Ry atom array. Furthermore, the scheme enables probing different phases by adjusting accessible experimental parameters, such as Ω and Δ , which effectively tune J (see [eq. \(6\)](#)). Implementing this model would mark a significant step toward realising the plaquette interactions that are central to lattice gauge theories.

1.3 Why Strontium?

So far, we have mainly focused on theoretical considerations, yet a key practical aspect shapes the experimental design and its complexity: the choice of atomic species. The main requirement of the proposal in [Section 1.2](#) is to achieve a large and tunable Rabi frequency for the Ry transition, as the coupling strength, J (see [eq. \(6\)](#)), must span a broad range to access the system's various phases. Besides, a large Ω also ensures higher fidelity in state preparation by mitigating decoherence effects. To meet this requirement, we employ strontium and its metastable clock state [[27](#)], which enables strong coupling to Ry states using readily available laser sources.

Specifically, we use the most abundant isotope, ^{88}Sr , a boson with zero nuclear spin and thus no hyperfine structure, which simplifies the experiment. Strontium's two valence electrons give rise to both singlet ($s = 0$) and triplet ($s = 1$) states. Transitions between these manifolds are, *a priori*, forbidden by the $\Delta s = 0$ selection rule but can become weakly allowed via spin-orbit coupling. One such transition connects the ground state $5s^2 \ ^1S_0$ to the excited state $5s5p \ ^3P_0$, commonly referred to as the clock state. This transition is doubly forbidden, also violating $\Delta j = \pm 1$, resulting in an exceptionally long state lifetime on the order of 10^{12} s ($\sim 10^3$ years) [[28](#)]. As this exceeds experimental timescales, atoms in 3P_0 do not decay, allowing it to serve as an effective ground state. We will discuss strategies to populate this level in [Section 2.1](#).

Using the clock state as an effective ground state enables single-photon excitation to a Ry state with commercially available lasers. In particular, we plan to use a frequency-doubled [[29](#)] 634 nm laser that provides 317 nm light. Due to the availability of sufficient optical power, such direct transition supports high Rabi frequencies (on the order of 10 MHz, as we will see in [section 2.2.1](#)). As a result, we will be able to achieve large and tunable J values.

If we were to perform single-photon excitation from the absolute ground state, we would require high-energy photons (middle to far UV), which are experimentally unfeasible. Furthermore, the transition selection rule $\Delta j = \pm 1$ would prevent straightforward access to n^3S_1 Ry states, which we intend to use.

Additionally, strontium is a well-established platform in ultracold atom experiments, with extensively studied transitions for cooling, trapping and imaging [30–32]. Moreover, our group previously set up a strontium-based quantum simulator, allowing us to leverage existing expertise and infrastructure to accelerate the development of the new experiment.

Briefly, strontium’s rich electronic structure, the availability of the long-lived clock state, which in turn enables single-photon Ry excitation, and our group’s prior expertise with this atomic species make it an ideal choice for developing our Ry atom array experiment.

2 Atomic Properties and Interactions

This section presents the numerical calculations performed during this master’s thesis, along with the corresponding results. The analysis primarily focuses on the characterisation of the 3P_0 clock state and different 3S_1 Ry states of strontium. These results provide insight into several experimental requirements, including the efficient population of the clock state, the excitation to Ry levels and their lifetimes, the applicability of the assumptions underlying the theoretical proposal (Section 1.2), and the preparation of specific atomic pair configurations.

2.1 Magnetic Response of the Clock State

If we use the $5s5p\ ^3P_0$ state as an effective ground state, a reliable method to populate it is essential. Due to its long lifetime, this level has a remarkably narrow linewidth, indicating a reduced frequency uncertainty of the transition. This narrow linewidth is also related to a small dipole matrix element, implying that the transition is weakly coupled to electromagnetic fields [33]. Consequently, the direct excitation to the clock state is challenging to achieve.

Multiple excitation schemes appeared to overcome this limitation: magnetic-field-induced 1-photon excitation [34], coherent 3-photon excitation [35], incoherent 3-photon pumping [36], and coherent (1+2)-photon excitation [37]. Incoherent pumping offers a straightforward implementation but is not efficient enough for high-fidelity state preparation. Therefore, we opt for a hybrid approach, combining it with magnetic-field-induced excitation, as demonstrated by the group of M. Endres [34].

Applying a magnetic field induces a slight mixing of the clock state with the nearby $5s5p\ ^3P_1$ state. Since the $5s^2\ ^1S_0 \rightarrow 5s5p\ ^3P_1$ transition is allowed, the mixing results in a weak effective coupling between the ground state and 3P_0 . To quantify this phenomenon, we analysed the Zeeman effect on the 3P_j manifold ($j \in \{0, 1, 2\}$) using exact diagonalisation (see Annex A for details on the calculations).

First, from the mixing between states, we extracted the linewidth of the $5s^2\ ^1S_0 \rightarrow 5s5p\ ^3P_0$ transition as a function of the magnetic field (Figure 2a). As discussed above, this quantity characterises the transition’s broadening and its experimental accessibility. Our results show that it increases to the 0.1 mHz range, corresponding to a lifetime on the order of $1/(0.1\ \text{mHz}) \sim 10^4\ \text{s}$. Thus, the transition remains sufficiently narrow, as a long lifetime is essential for using the clock state as an effective ground state. At the same time, the slight broadening is enough to improve the efficiency of direct excitation.

For comparison, we included the result from perturbation theory (PT) [38, 39]. Given its agreement, we note that exact diagonalisation is not required even for large fields.

To assess the coupling strength to the clock state, we calculated the Rabi frequency of the excitation as $\hbar\Omega = \langle \Psi_{\text{clock}} | -\hat{\mathbf{d}} \cdot \mathbf{E} | ^1S_0 \rangle$. PT yields $\Omega \propto B$ and, since $|\mathbf{E}|$ is related to the field’s intensity, $|\mathbf{E}| \propto \sqrt{I}$, we can separate a coefficient independent of experimental

parameters¹: $\Omega = \tilde{\Omega} \cdot \sqrt{I} \cdot B$. Our results show $\tilde{\Omega} = 99.8 \text{ Hz} \cdot \sqrt{\text{cm}^2/\text{mW}} \cdot 1/\text{T}$, in good agreement with the literature [39]. For a typical intensity² of $5 \cdot 10^3 \text{ mW}/\text{cm}^2$, the Rabi frequency is on the 0.1 kHz range (Figure 2b). Although this coupling is relatively weak, it is sufficient as the excitation will be faster than the lifetime of the level and of atoms in the optical traps (on the order of s).

Finally, Figure 2c shows the energy shift of the clock state as a function of the magnetic field. At 10^3 G , the shift reaches 0.23 MHz. Given that acousto-optic modulators offer a frequency tunability on the order of 10 MHz [40], the transition remains addressable with a single laser across all the B field values that we considered.

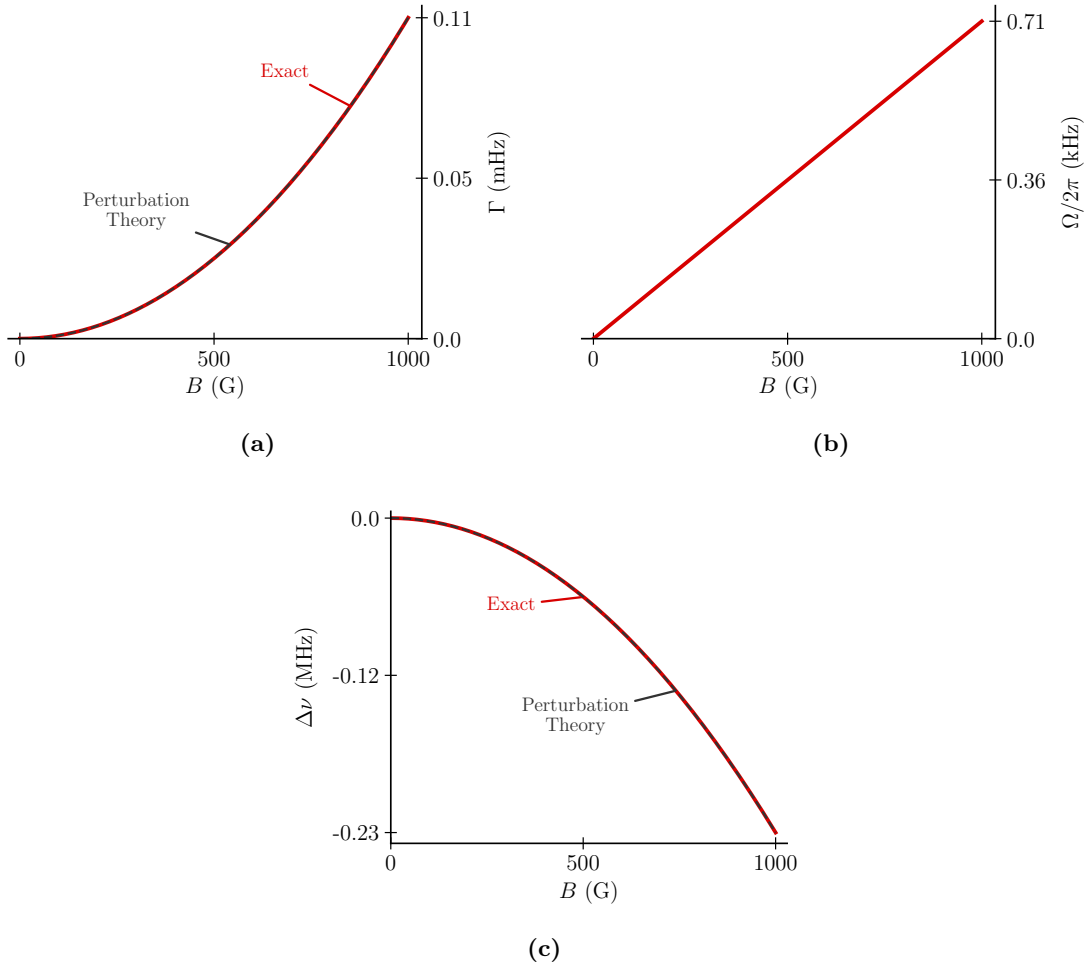


Figure 2: (a) The linewidth of the $5s^2 \ ^1S_0 \rightarrow 5s5p \ ^3P_0$ transition increases quadratically with the magnetic field, B , as predicted by PT, and reaches the mHz range. (b) The Rabi frequency grows linearly with B , as expected from PT, and is in the range of 0.1 kHz for a typical intensity of $5 \cdot 10^3 \text{ mW}/\text{cm}^2$. (c) The energy of $\ ^3P_0$ shifts downwards on the 0.1 MHz range, lowering quadratically with B as predicted by PT.

¹It would still depend on the field's polarisation. We always assume π -polarised light.

²For a Gaussian beam: $I = 2P/\pi w^2$, where P is the power and w is the waist radius. For typical parameters, we expect $P = 5 \text{ mW}$ and $w = 250 \text{ }\mu\text{m}$.

2.2 Characterisation of Rydberg states

Another key consideration is the choice of the Ry state. To guide this decision, we analysed the properties of $5sns\ ^3S_1$ states for $n \in [40, 100]$, dividing the study into two parts: single-atom properties, focusing on lifetimes and transition strengths; and Ry-Ry interactions as a function of the principal quantum number, n , and the interatomic distance.

2.2.1 Lifetimes and Rabi Frequencies

The spectrum of Ry atoms is accurately described using a phenomenological extension of the hydrogen atom model. In this approach, the hydrogen's energy levels, $E_n \propto 1/n^2$, are modified by replacing the principal quantum number with the effective value $n^* = n - \delta_l$, where δ_l is the quantum defect. This parameter depends primarily on the orbital angular momentum quantum number, l , and is determined empirically. Incorporating these modified eigenenergies introduces an effective potential into the Hamiltonian. Diagonalising this Hamiltonian yields the Ry wave functions, from which one can derive properties such as lifetimes and Rabi frequencies [14, 41].

The implementation of quantum defect theory is readily available in multiple Python packages. First, we used `pairinteraction` [42] to compute the lifetimes of the Ry states at 300 K. As shown in Figure 3a, the values are on the order of 100 μs and increase with n . These results should be interpreted with caution, as calculations for alkaline-earth species may not fully capture inter-electron correlations and omit specific experimental decoherence mechanisms [43]. Nevertheless, they reproduce the expected scaling behaviour, $n^3 \cdot 10^{-9}$ s [14, 44], providing an initial estimate of the order of magnitude.

Next, using the `ARC` package [43], we computed the Rabi frequencies for the transitions $5s5p\ ^3P_0 \rightarrow 5sns\ ^3S_1$ and a typical intensity³ of $5 \cdot 10^5$ mW/cm² (Figure 3b). The results range from 17.5 MHz at $n = 40$ to 9.1 MHz at $n = 100$. These values are large and scale with the square root of the laser power, offering flexibility to tune the interaction strength J (see eq. (6)) and explore the different phases of the model. Additionally, the Rabi frequency scales as $n^{-3/2}$, as expected, since Ω is proportional to the square root of the linewidth, which is the inverse of the lifetime [45, Chapter 2.2].

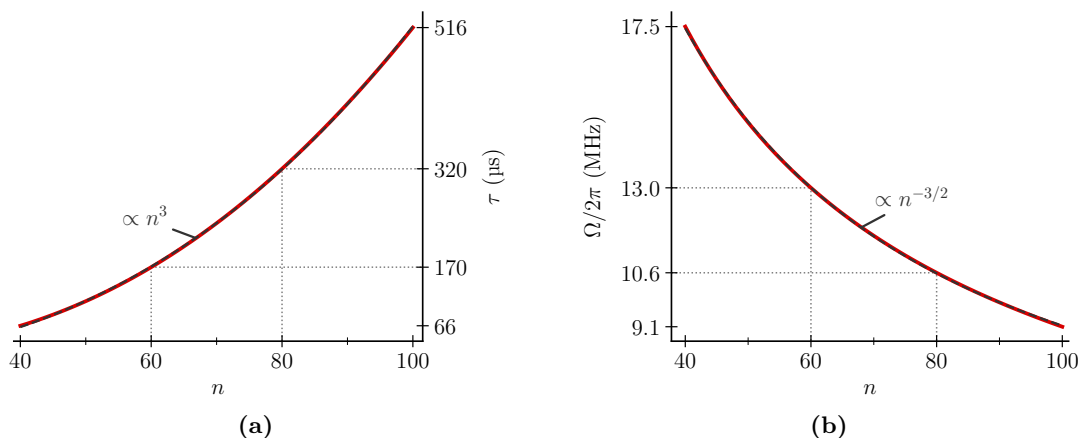


Figure 3: (a) The lifetime of Ry states, $5sns\ ^3S_1$, increases cubically with the principal quantum number, n , and is on the order of 100 μs . (b) The Rabi frequency of the transition, $5s5p\ ^3P_0 \rightarrow 5sns\ ^3S_1$, decreases as $n^{-3/2}$ and is in the range of 10 MHz for a typical intensity of $5 \cdot 10^5$ mW/cm².

³In this case, we expect $P = 500$ mW and $w = 250$ μm .

The π -pulse time associated with these Rabi frequencies, π/Ω , lies in the 100 ns range, which is fast enough to ensure high-fidelity preparation of Ry states. If the excitation was slower, differences in the Rabi frequency across the atomic ensemble could lead to dephasing, preventing all the addressed atoms from being in the $|r\rangle$ state.

Lastly, also with the ARC package, we extracted the wavelengths of the $5s5p\ ^3P_0 \rightarrow 5sns\ ^3S_1$ transitions, corresponding to the eigenenergies modified by the quantum defect. These range from 317.1 nm at $n = 40$ to 316.4 nm at $n = 100$, thereby spanning 0.7 nm. If we desire to address different Ry states, we must consider this variation to ensure the laser source has sufficient tuning range.

2.2.2 Rydberg-Rydberg Interactions

As outlined in [Sections 1.1](#) and [1.2](#), the Ry blockade radius constrains the lattice geometry in the planned experiment. Moreover, the proposal assumes that the Ry-Ry interaction is of the form C_6/r^6 . Nonetheless, this assumption relies on the validity of the perturbative regime. Assuring we can apply it requires a detailed study of the Ry interaction.

To solve Ry interactions exactly, as outlined in [Section 1.1](#), one would diagonalise the full Hamiltonian, including the entire multipole expansion and atomic spectrum. This is intractable, so simplifications are necessary. One approach is to truncate both the expansion and the basis. Alternatively, for analytical expressions, one can apply PT to the leading order of the multipole expansion, yielding the van der Waals potential ([eq. \(3\)](#)). Both methods are within the `pairinteraction` Python package, which we used to characterise the Ry-Ry interactions of the $5sns\ ^3S_1$ states for $n \in [40, 100]$ (see details in [Annex B](#)).

We began by calculating the perturbative C_6 coefficients. Using these results, we computed the Ry blockade radius, defined as $R_b = \sqrt[6]{C_6/\hbar\Omega}$, for realistic Rabi frequencies: $\Omega \in \{1, 5, 20\}$ MHz (see [Section 2.2.1](#)). With the resulting values, we explored the allowed lattice geometries. As introduced in [Section 1.2](#), the two atoms at each site must be at a distance $\eta < R_b$, ensuring only one atom can be excited at a time. Due to diffraction effects, they also cannot be placed closer than 1 μm . Meanwhile, the distances between different pairs must satisfy $d, e, f > R_b$. To simplify the analysis and reduce the number of degrees of freedom, we fixed $\Omega = 5$ MHz, $d = f$ and $\theta_d = \theta_f = 45^\circ$. Under these constraints, we imposed $F(\mathbf{d}, \boldsymbol{\eta}) = -2F(\mathbf{e}, \boldsymbol{\eta})$ to identify geometries compatible with the proposed model. Additionally, we assured that nearest-neighbour interactions were stronger than the next-nearest-neighbour ones, as the opposite would invalidate the mapping.

We present the results in [Figure 4a](#). For larger n , the number of compatible geometries increases rapidly. This trend arises from the Ry blockade radius also growing with n (as shown in [Figure 4c](#)), allowing for a broader range in η and, thus, more valid parameter combinations. We also expected the saturation for $n \approx 80$. As n and R_b increase, the lattice expands due to the constraint $d, e > R_b$. However, we set $d, e \leq 30\ \mu\text{m}$, reflecting experimental limits on lattice size and site number, so not all larger geometries are included.

As discussed in [Section 1.1](#), it is crucial to identify when the perturbative interaction regime ([eq. \(3\)](#)) breaks down. To this end, we carried out the exact diagonalisation of the truncated multiple expansion with a restricted basis. This calculation yielded a spectrum for each n , as the one in [Figure 4b](#), displaying the overlap between the initial pair state and the resulting eigenstates as a function of the interatomic distance. As the atoms approach, the initial state begins to mix significantly with other levels, and the energy no longer follows the van der Waals potential. This deviation signals the failure of PT.

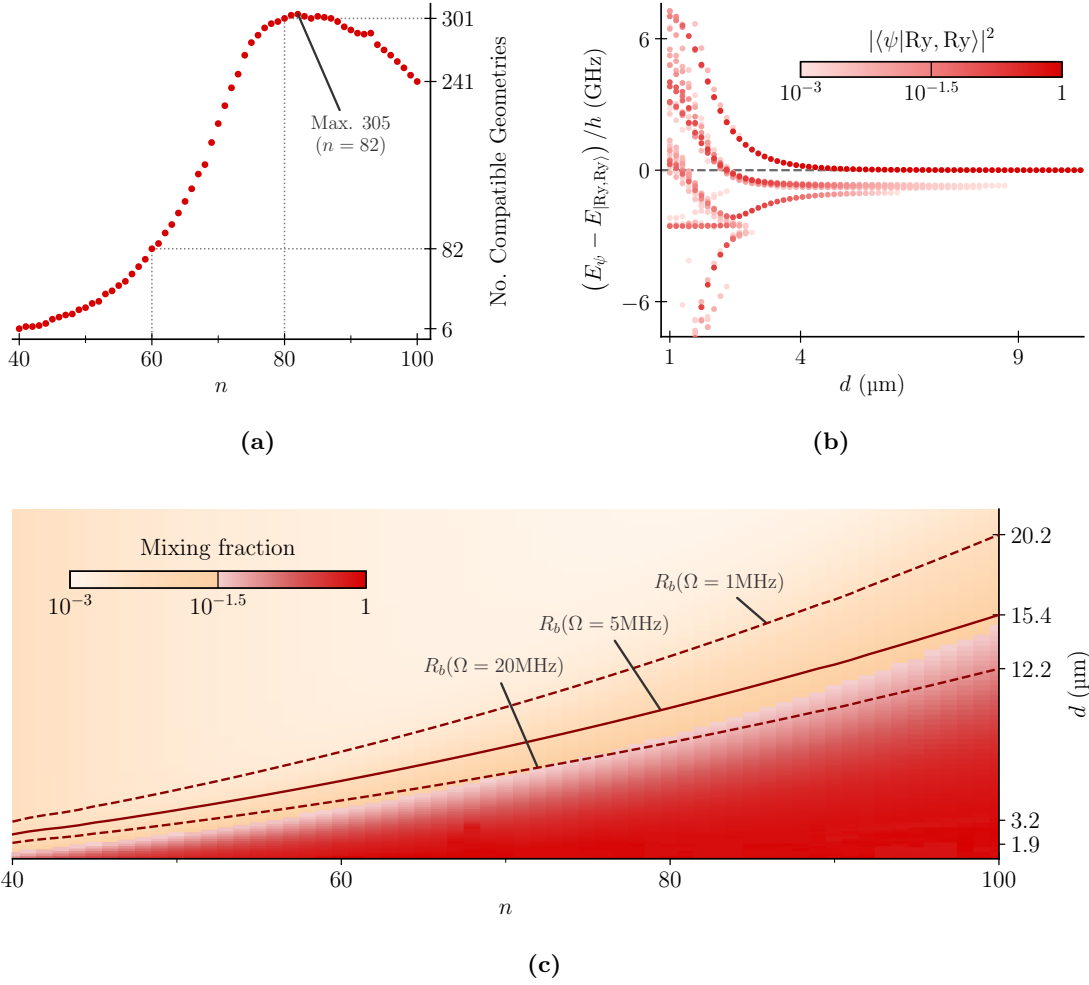


Figure 4: (a) The number of valid lattice geometries, under the constraints of the proposal in Section 1.2, increases with the principal quantum number, n , saturating due to the parameter upper limits. (b) The diagonalised Ry-Ry interaction spectra reveal how the initial pair state, $|\text{Ry}, \text{Ry}\rangle$ (here $5s70s\ ^3S_1$), mixes with nearby levels, $|\psi\rangle$. The vertical axis shows the energy difference between $|\psi\rangle$ and $|\text{Ry}, \text{Ry}\rangle$, while the colour indicates their overlap. Only for $d > 9\ \mu\text{m}$ does $|\text{Ry}, \text{Ry}\rangle$ remain unmixed. (c) As n increases, Ry pair states start to mix significantly at larger distances, even beyond experimentally accessible Ry blockade radii.

In Figure 4c, we plot the mixing fraction of each $5sns\ ^3S_1$ state, *i.e.*, the extent to which the original pair state spreads to other levels, as a function of the interatomic distance and the principal quantum number. We also overlay the computed Ry blockade radii for different Rabi frequencies. For the model presented in Section 1.2 to remain valid, interactions between sites must be of the form C_6/R^6 . This regime is only applicable when the target Ry state remains effectively unmixed with nearby levels. As a result, the allowed lattice geometries are further constrained: all distances (η , d , e) must exceed the threshold at which mixing becomes significant. At the same time, η must remain smaller than the Ry blockade radius, so ideally, mixing should start well below R_b . Within the range of Rabi frequencies considered, we find that this is not the case for high- n states. Solely for $n < \sim 70$, it is possible to access values of η that fall below the Ry blockade and avoid significant mixing, even with $\Omega = 20\ \text{MHz}$.

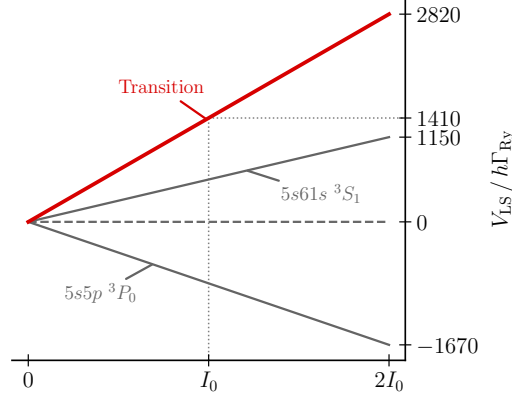


Figure 5: The clock, $5s5p\ ^3P_0$, and Ry state, $5s61s\ ^3S_1$, shift oppositely and at different rates as a function of the intensity of 813 nm light. The differential light shift is non-zero, so the transition frequency offsets by several linewidths. As a reference, we use the tweezer’s intensity for a trap depth of 0.5 mK, $I_0 = 7.8 \cdot 10^8\ \text{mW/cm}^2$.

2.3 Light Shifts and Selective Rydberg Excitation

The final theoretical aspect we address concerns state preparation. As described in [Section 1.2](#), each atomic pair encodes a single spin, depending on whether the right or left atom is excited. Thus, preparing specific initial states requires the ability to excite each atom of the pair individually. For example, to initialise the fully flippable phase, where all spins are aligned, either all left or all right atoms must be excited.

To trap the atoms, we will use optical tweezers, which are tightly focused laser beams that create potential minima via the AC Stark effect [[11](#), [12](#), [38](#)]. The resulting energy offset, or light shift, is given by the operator $\hat{V}_{\text{LS}} = -\hat{\alpha}|\mathbf{E}|^2$, where \mathbf{E} is the electric field’s complex amplitude and α is the state’s frequency-dependent polarisability. In our case, we use 813 nm light, known as a magic wavelength, for which the polarisabilities of the absolute ground state and the clock state are equal. As a result, both states undergo the same energy shift, leaving the transition frequency unchanged upon light intensity fluctuations and thereby improving the fidelity of clock-state preparation.

We can also exploit this light shift effect to achieve selective excitation. By adjusting the laser intensity ($I \propto |\mathbf{E}|^2$) at each atom’s position, we can shift one atom’s Ry level out of resonance, allowing control over which atoms are excited [[46](#)].

The key quantity in this context is the differential light shift between the clock state and the Ry state. If both shift equally, the transition remains resonant, as with the ground and clock states. For proof-of-principle calculations, we considered the $5s61s\ ^3S_1$ Ry state. We first computed the polarisabilities, α , of the clock and Ry states for 813 nm light. These were obtained using PT applied to $\hat{V} = -\hat{\mathbf{d}} \cdot \mathbf{E}$, yielding an expression for α that depends on experimental data (see details of the calculation in [Annex C](#)).

Then, we calculated the differential shift of the transition as a function of the laser’s intensity, since $|\mathbf{E}|^2 \propto I$, and relative to the Ry state’s linewidth:

$$\frac{\Delta V_{\text{LS}}}{h\Gamma_{\text{Ry}}} = \frac{V_{\text{LS}}^{\text{Ry}} - V_{\text{LS}}^{\text{clock}}}{h\Gamma_{\text{Ry}}} = \mathcal{C} \frac{\alpha_{\text{Ry}} - \alpha_{\text{clock}}}{h\Gamma_{\text{Ry}}} I, \quad (9)$$

where \mathcal{C} is a scale factor. We assumed a linewidth of $\Gamma_{\text{Ry}} = 1/80\ \mu\text{s}^{-1}$ [[34](#)] and an intensity range around $I_0 = 7.8 \cdot 10^8\ \text{mW/cm}^2$, which corresponds to a tweezer depth of 0.5 mK⁴.

⁴We expect atoms to be at around $\sim 2\ \mu\text{K}$, so the tweezer must be considerably deeper to trap them. To

The results show that, even for slight variations in the tweezer’s intensity, the shift is of several linewidths (Figure 5), indicating the transition will be detuned from resonance. Furthermore, at I_0 , we obtain a shift of 18 MHz ($1410\Gamma_{\text{Ry}}$), which matches the experimental value in the literature [38].

2.4 Conclusions and Outlook

In summary, we started by analysing the clock excitation scheme. We showed that applying a magnetic field broadens the otherwise forbidden $5s^2\ ^1S_0 \rightarrow 5s5p\ ^3P_0$ transition while leaving its frequency practically unchanged. As a result, the clock state can be populated by employing a single-photon excitation.

Next, we focused on characterising Ry states and the validity of the van der Waals regime over a wide range of principal quantum numbers ($n \in [40, 100]$). High- n states allow for greater flexibility in lattice geometries that satisfy the model constraints (note that we did not include geometric restrictions regarding state mixing). However, lower- n states seem more favourable, as they support larger Rabi frequencies (*i.e.*, larger J , see eq. (6)) and maintain a reasonable region below the Ry blockade radius where mixing remains negligible. Since the lifetimes are long enough for all n values, the main factors in selecting an optimal Ry state are the achievable coupling strengths and available lattice geometries. In practice, intermediate n values, between 50 and 70, seem the most compelling candidates. For instance, the $5s61s\ ^3S_1$ state may be a strong option, given its prior experimental use and the availability of supporting literature [34].

Finally, using the $5s61s\ ^3S_1$ state, we verified that adjusting the trap intensity can shift atoms out of resonance. This effect, combined with varying intensities across optical tweezers, would enable selective excitation within atomic pairs.

Moving forward, a few relevant tasks remain. First, Ry-Ry interactions are extremely sensitive to electric fields [42, 47]. Hence, it will be necessary to incorporate the effect of typical stray electric fields in the experiment into the calculations presented in Section 2.2.2. These perturbations could limit our ability to prepare high- n Ry states. Furthermore, once we can reliably trap atoms in optical tweezers, it will be essential to validate our predictions, including those on the blockade regime, the C_6 coefficient, and the lifetimes.

3 The Red Laser System

This section outlines the experimental work carried out during this master’s thesis, including the setup of the main paths for the 689 nm red laser system, the construction and locking of a slave diode for the red 3D magneto-optical trap (MOT), and the characterisation of an ultrastable cavity intended for stabilising the red lasers. Annex E includes pictures of all the setups discussed throughout this section.

3.1 Overview of the Experiment

Before analysing the details, it is insightful to provide a global view of the experiment [48]. Everything takes place inside an ultra-high-vacuum chamber, which ensures the isolation of strontium atoms by limiting collisions with other background atoms. The sequence starts at the oven, where solid strontium is heated to generate an atomic jet. This atomic flux is then cooled using transverse cooling and slowed down by a Zeeman slower. Afterwards, the atoms are trapped and cooled further in a blue 2D MOT before being pushed to a glass

extract the intensity, one uses $k_B T = V_{\text{LS}}^{\text{clock}} = C\alpha_{\text{clock}}I_0$, where k_B is the Boltzmann constant.

cell, which is yet to be installed, where a blue 3D MOT will capture them. All these laser cooling and trapping techniques (for more details, see [45, 49]) are operating on the strong $5s^2\ ^1S_0 \rightarrow 5s5p\ ^1P_1$ transition at 461 nm. At this stage, atomic temperatures will reach a few mK. To achieve the μK regime, we will use a second red 3D MOT on the narrow $5s^2\ ^1S_0 \rightarrow 5s5p\ ^3P_1$ transition at 689 nm.

Once cold enough to be trapped by the optical tweezers, the atoms will be loaded into a configurable array generated with 813 nm light. They will then be excited to the clock state using a laser at 698 nm, followed by Ry excitation with a high-power UV laser at 317 nm. At the end of the experimental sequence, atoms will be imaged while active Sisyphus cooling at 689 nm will keep them trapped.

In this master’s thesis, we focused on setting up the 689 nm laser system. Because a single laser source must serve multiple purposes, it was necessary to build optical paths to distribute the light through fibres to different parts of the experiment (Figure 6). Specifically, the 3D MOT and Sisyphus cooling require 689 nm light. An additional path is also needed to stabilise the laser using an ultrastable cavity, as detailed in Section 3.3

These main paths are relatively straightforward, consisting primarily of mirrors, polarising beamsplitters (PBS) and waveplates (WP) to split and guide the laser light. Setting them up is mainly a matter of optical alignment. Nonetheless, two noteworthy considerations arose: polarisation fluctuations and the use of acousto-optic modulators.

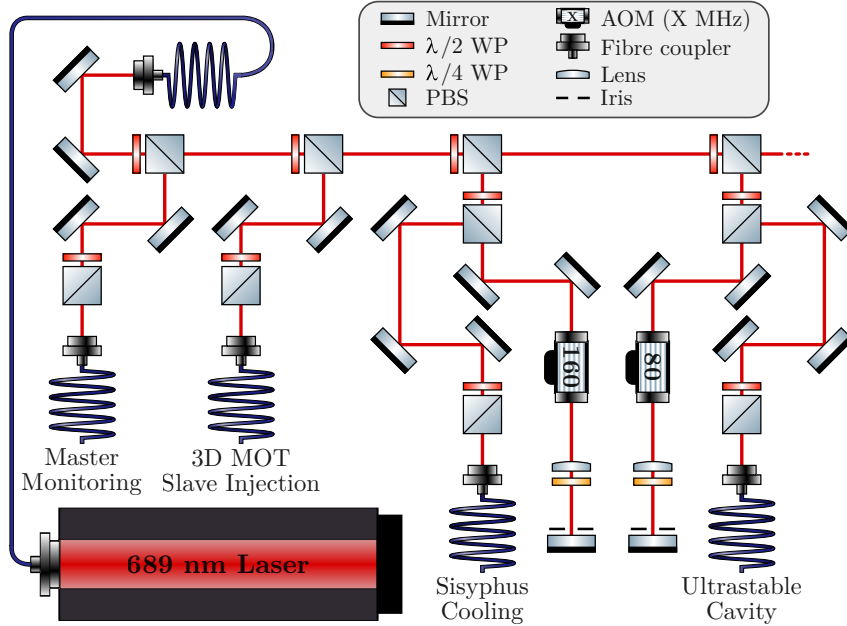


Figure 6: The setup for the main optical paths distributes light across the experiment using fibres.

3.1.1 Polarisation Fluctuations in the 689 nm Laser

First, since coupling light to fibres involves continuous power monitoring, we were able to detect fluctuations in optical power even when the setup remained unchanged. These fluctuations only appear after the light passes through polarising elements, such as polarising beamsplitters and waveplates, and not directly at the laser output. This behaviour points to polarisation rotation as a likely cause. As laser cooling and trapping rely on well-defined polarisation, such fluctuations pose a critical issue that remains to be addressed.

3.1.2 Frequency Tuning with Acousto-Optic Modulators

Second, we use acousto-optic modulators (AOMs) in several optical paths. These devices consist of a crystal in which a piezoelectric transducer generates sound waves. The resulting pressure waves modulate the crystal’s refractive index, leading to Bragg diffraction of the incoming light [40]. Each diffracted order undergoes a frequency shift determined by the driving signal, enabling precise control over the light’s wavelength delivered to specific parts of the experiment. To compensate for the angular deviation introduced by diffraction as we sweep the frequency, all AOMs operate in a double-pass configuration [50], preserving the original propagation direction. Additionally, since we align the setup for a specific diffraction order, turning the AOMs on or off misaligns the beam, effectively acting as fast optical switches. Moreover, tuning the power of the driving signal controls the diffraction efficiency, allowing us to also use AOMs as variable optical attenuators.

In our setup, the 689 nm laser drives the $5s^2\ ^1S_0 \rightarrow 5s5p\ ^3P_1$ atomic transition while being coupled to the resonance of an ultrastable cavity. Ideally, the laser frequency should be close enough to the transition so that a single AOM can bridge the remaining detuning. Since AOMs introduce significant intensity losses, we aim to minimise their use in paths which deliver light directly to the atoms and demand optical power. However, tuning the laser close to the atomic resonance can ultimately place it far from any cavity mode. For this reason, we use additional AOMs in the path to the ultrastable cavity to bridge the frequency gap. In this case, power loss is not a concern, as only a small amount of light ($< 100\ \mu\text{W}$) is needed to couple to the cavity.

3.2 Power Amplification with a Slave Diode

To achieve an effective red MOT, we require tens of mW of optical power. However, the 689 nm laser supplies only around 15 mW, which are spread across several paths. To overcome this limitation, we use a slave diode, a high-power laser diode ($\sim 50\ \text{mW}$) with a broader emission spectrum than the 689 nm master laser. By injecting a small amount of light from the master into the slave, we induce injection locking, causing the slave to lase at the same frequency as the master with a fixed phase offset [51]. With this technique, we effectively amplify the available power for the red 3D MOT.

3.2.1 Setup

We depict the slave laser setup in [Figure 7a](#). Light from the master laser is injected into the slave, and the output splits between the experiment and a monitoring setup. Again, we use an AOM to tune the light’s frequency to the atomic transition.

A key component of this setup is the Faraday isolator, which ensures unidirectional propagation of light. This device relies on the rotation of polarisation by a magnetic field, known as the Faraday effect [52], to block any back-reflected light. Input and output polarisers are set at 45° relative to each other, matching the polarisation rotation induced by the isolator. As a result, forward-propagating light transmits, while reflected light accumulates a total rotation of 90° , becoming orthogonal to the input polariser and thus blocked [53]. In our setup, the isolator prevents reflections that could affect the stability of the master laser.

Additionally, the slave’s output beam does not display the desired Gaussian intensity profile, TEM_{00} [54], but an elongated transverse mode ([Figure 7b](#)). To correct this, we use a cylindrical telescope that focuses the long axis and recovers a circular profile ([Figure 7c](#)).

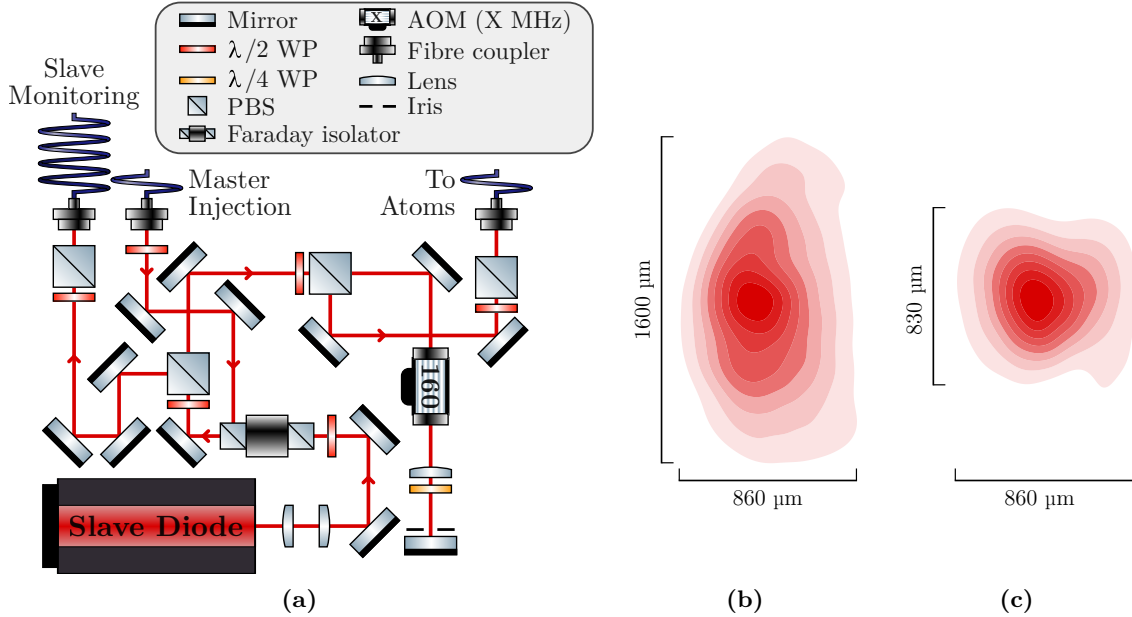


Figure 7: (a) The setup for the slave diode allows injecting light from the master to amplify the 3D MOT's power. (b) The measured intensity profile of the slave's beam is elongated. (c) The cylindrical telescope in the setup corrects the intensity profile to resemble the TEM_{00} mode.

3.2.2 Monitoring with an Optical Cavity

As briefly introduced in Section 3.2.1 and shown in Figures 6 and 7a, a portion of light from the master and the slave lasers is sent to a monitoring system (Figure 8a) and coupled to a cavity. This setup allows us to initially injection-lock the slave and verify that it remains locked over time.

Before detailing the locking procedure, it is useful to briefly review the physics of optical cavities [54–57], which will also be relevant in Section 3.3. In our case, we use a Fabry-Pérot cavity consisting of two highly reflective mirrors facing each other and separated by a distance L . Constructive interference occurs when L is an integer multiple of half the wavelength of the incident light:

$$L = n \frac{\lambda}{2}, \text{ with } n \in \mathbb{Z}. \quad (10)$$

When this condition is satisfied, light builds up inside the cavity, and a fraction of it leaks through the mirrors. The frequencies for which this happens are the cavity's resonances and correspond to transmission maxima (Figure 8b). The spacing between resonances, known as the free spectral range (FSR), is a characteristic parameter of the cavity:

$$\Delta\nu_{\text{FSR}} = \frac{c}{2L}. \quad (11)$$

In addition to longitudinal resonances, one must consider the transverse modes of the cavity beyond TEM_{00} , *i.e.*, the different transverse intensity profiles. These can be excited if the incoming beam is misaligned or contains higher-order spatial modes. These transverse modes are slightly detuned from the fundamental resonance and appear as additional peaks in the transmission spectrum (Figure 8b). To ensure efficient coupling and suppress excitation of higher-order modes, a lens can be placed before the cavity to match the beam's profile to that of the cavity's TEM_{00} mode.

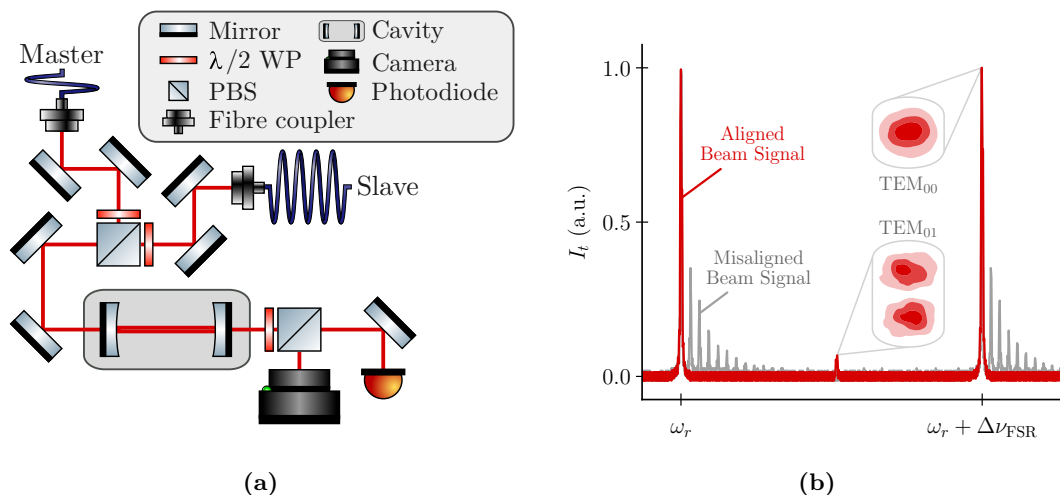


Figure 8: (a) The setup for monitoring allows checking on the master and verifying the slave’s injection lock by coupling their light to a Fabry-Pérot cavity. (b) The measured cavity’s transmission spectrum displays sharp peaks at the resonance frequencies. Additional peaks arise from beam misalignment, indicating excitation of higher-order modes. Even when well aligned, a small coupling to the TEM_{01} mode is hard to avoid.

Another key parameter is the full width at half maximum (FWHM) of the resonance peaks, $\Delta\nu_{\text{FWHM}}$, which depends on the mirrors’ reflectivity. Higher reflectivity leads to more internal reflections, enhancing destructive interference for off-resonant light. Thus, only light with a frequency closer to the resonance is transmitted, producing narrower transmission peaks. The FWHM links to the FSR through the finesse, \mathcal{F} , which also relates to the mirrors’ intensity reflection coefficient, R :

$$\mathcal{F} = \frac{\Delta\nu_{\text{FSR}}}{\Delta\nu_{\text{FWHM}}} = \frac{\pi\sqrt{R}}{1-R}. \quad (12)$$

A higher finesse corresponds to narrower resonances and greater frequency resolution. Note that \mathcal{F} may vary with wavelength, depending on the mirror coatings.

In our monitoring setup, we use a low-finesse cavity with $\mathcal{F} \approx 313$ ($R = 0.99$). One of the mirrors is mounted on a piezoelectric transducer, allowing us to scan the cavity length and bring it into resonance with the laser without modulating the frequency itself. To measure the transmission spectrum, we use a photodiode at the output. Additionally, a camera allows us to observe the transverse mode structure of the transmitted light (insets in Figure 8b).

To lock the slave laser, we couple light from the slave into the cavity and adjust the diode’s current setting until its transmission spectrum shows a single peak. This signal indicates that the slave has synchronised with the master and is injection-locked. As a reference, we also couple light from the master, which shows a peak at the same frequency as the slave, as expected.

3.3 Frequency Stabilisation with an Ultrastable Cavity

The final setup we discuss concerns the stabilisation of three lasers in the experiment: those operating at 634 nm, 689 nm and 698 nm. Each addresses a narrow atomic transition. The 634 nm laser, after frequency doubling [29], generates the 317 nm light for Ry excitation, where the transition has a linewidth on the order of kHz (see Section 2.2.1). The 689 nm

laser drives the $5s^2\ ^1S_0 \rightarrow 5s5p\ ^3P_1$ intercombination line, which also has a linewidth of a few kHz [58]. Finally, the 698 nm laser addresses the extremely narrow clock transition, whose linewidth is on the order of mHz (see Section 2.1).

It is crucial to suppress frequency fluctuations in the lasers to prevent them from drifting out of resonance. To achieve this, we lock the lasers to an ultrastable Fabry-Pérot cavity⁵, which acts as a high-resolution frequency reference [59, 60]. This stabilisation also reduces the lasers' linewidths, ensuring that a greater fraction of the optical power is resonant with the atomic transition and thus improving excitation efficiency.

To ensure stability, the cavity is built around an ultra-low expansion glass spacer, which sets the mirror separation. It is housed in a vacuum chamber designed for thermal and mechanical isolation and will rest on a vibration-isolation platform. Active temperature control maintains the setup at the so-called zero-crossing temperature, where the thermal expansion coefficient, $\alpha(T)$, vanishes. As a result, thermal fluctuations do not induce changes in the length of the cavity, as $\Delta L = \alpha(T) \cdot \Delta T$ becomes negligible [61].

In our case, the ultrastable cavity should offer a finesse of $\sim 1.7 \cdot 10^5$ at 698 nm. Due to the mirrors' coating, this value is similar at 689 nm but is expected to drop to $\sim 4 \cdot 10^4$ at 634. However, high finesse is especially crucial for the 698 nm laser, given the extreme narrowness of the clock transition. For the other lasers, a lower finesse would suffice.

3.3.1 Characterisation of the Ultrastable Cavity

Once the cavity was in place and the vacuum was re-established after shipping, we assembled a temporary setup to characterise it (Figure 9a). Our main goal was to verify that the finesse matched the manufacturer's specifications. Since we expected the highest finesse at 698 nm, but only the 689 nm laser was available during the measurement, we anticipated a value slightly below $1.7 \cdot 10^5$.

In this cavity, the length is fixed, so we must identify resonances by scanning the laser frequency. We achieve this by tuning the piezoelectric transducer within the laser. Assuming a linear frequency scan, $\omega = \omega_0 + \alpha t$, one can derive the expression for the cavity's reflected intensity (see Annex D). The resulting signal exhibits a characteristic chirped oscillation, *i.e.*, of increasing frequency, modulated by an exponential decay (Figure 9b):

$$I_r \propto e^{-t/\tau} u(t), \quad (13)$$

where $u(t)$ is the chirped oscillation, and the cavity decay time is $\tau^{-1} := \Delta\nu_{\text{FSR}}(1 - R)$.

We can intuitively understand the shape of this reflection spectrum. Initially, when the laser is off-resonance, all the light is reflected. As the scan brings the laser into resonance with the cavity, reflection dips significantly as light couples to the cavity and transmits. Once the laser goes out of resonance, the reflected signal results from the interference of two fields: the instantaneous reflection at $\omega(t)$ and the residual cavity leakage at the fixed resonance frequency. The beating between these two produces the chirped oscillations, while the exponential decay reflects the gradual leakage of the field inside the cavity [59].

We extracted the cavity decay time, τ , by fitting the exponential envelope of the reflected signal. Given the known cavity length of $L = 12.1$ cm, the FSR is set at $\Delta\nu_{\text{FSR}} = 1.24$ GHz. Using these values and the measured τ , we determined the mirrors' reflectivity, R , and calculated the finesse. From eight measurements like the one shown in Figure 9b, we obtained $\tau = (42.32 \pm 0.96)$ μs , corresponding to a finesse of $\mathcal{F} = (1.647 \pm 0.037) \cdot 10^5$, consistent with the expected value of $\sim 1.7 \cdot 10^5$.

⁵MenloSystems, ORC-Cylindric.

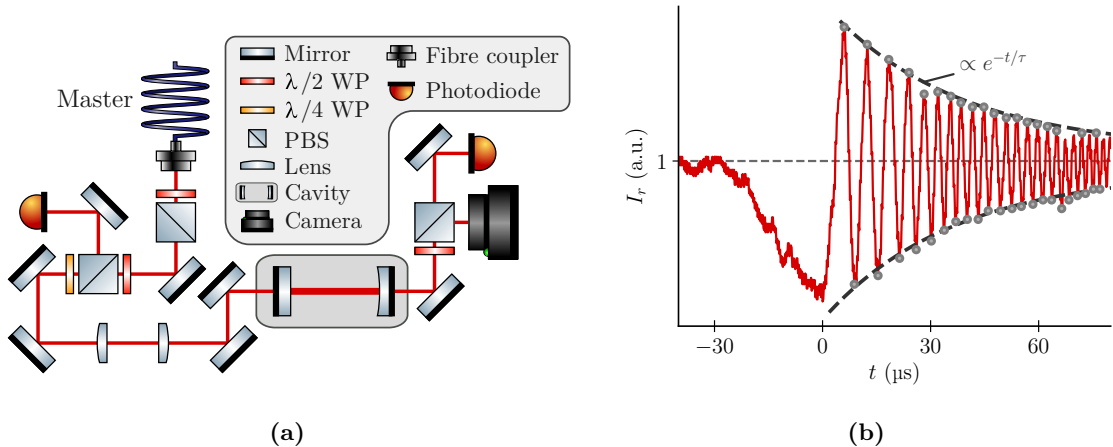


Figure 9: (a) The temporary setup for characterising the cavity allows obtaining the finesse from measuring the reflection signal. (b) By fitting the exponential decay of the chirped oscillations in the measured reflection signal, we obtain the lifetime of the cavity.

3.3.2 Pound-Drever-Hall Technique for Frequency Stabilisation

With the cavity characterised, we were ready to stabilise the 689 nm laser. However, due to time constraints, we could not complete this during the master’s thesis. Nonetheless, we tested the stabilisation procedure using the low-finesse cavity from the monitoring setup.

The goal of frequency stabilisation, or locking, is to ensure the laser remains resonant with the cavity by continuously correcting fluctuations. When done correctly, the laser’s linewidth reduces significantly, becoming narrower than that of the cavity. Among the various locking methods, the Pound-Drever-Hall (PDH) technique [62] is particularly robust, as it is insensitive to intensity fluctuations. Its core principle is to generate an error signal that indicates whether the laser drifts above or below the resonance.

To understand how PDH locking works, we outline the key steps of the derivation presented in [63]. Before entering the cavity, the laser light is modulated by an electro-optic modulator (EOM), which uses a crystal (lithium niobate in our case) whose refractive index varies with an applied voltage [64]. By driving the EOM with a voltage of the form $\beta \sin(\Omega t)$, the light’s phase is modulated as

$$E = E_0 e^{i[\omega t + \beta \sin(\Omega t)]}. \quad (14)$$

For small modulations ($\beta \ll 1$), we can expand the exponential and rewrite the sine in terms of complex exponentials:

$$E \approx E_0 e^{i\omega t} [1 + i\beta \sin(\Omega t)] = E_0 \left[e^{i\omega t} + \frac{\beta}{2} e^{i(\omega+\Omega)t} - \frac{\beta}{2} e^{i(\omega-\Omega)t} \right]. \quad (15)$$

This expression reveals that the light now contains three frequency components: the original carrier at ω , and two sidebands at $\omega \pm \Omega$.

When the carrier frequency is not exactly resonant with the cavity, the reflected light at ω interferes with the sidebands, generating a beating signal with multiple frequency components. Among these, the one oscillating at Ω encodes information about the laser’s drift from resonance, $\text{Err}(\omega)$. To extract it, we use a mixer, which is an electronic device that multiplies two input signals [65]. By feeding the reflected intensity and the original

modulation into the mixer, the output is

$$[\text{Err}(\omega) \sin(\Omega t) + O(2\Omega)] \cdot \sin(\Omega t) = \frac{\text{Err}(\omega)}{2} [1 - \cos(2\Omega t)] + O(\Omega). \quad (16)$$

Applying a low-pass filter, which removes all fast oscillations [66], isolates the constant term in eq. (16) and yields the error signal. As shown in Figure 10b, this signal crosses zero at resonance and changes sign on either side, effectively tracking the laser’s drifts. Note that the sidebands themselves also become resonant at specific frequencies, resulting in similar features in the signal.

To implement the PDH technique experimentally, we modified the slave-monitoring setup by introducing an EOM and adding a detection path for the cavity’s reflected light (Figure 10a). As part of this setup, particular attention must be drawn to the reflection photodiode. Since the error signal relies on extracting components oscillating at the modulation frequency, the photodiode must have sufficient bandwidth to resolve these variations.

To complete the locking loop, we used a laser controller with a built-in PDH module⁶ and a FALC pro⁷. The laser controller drove the EOM to apply phase modulation, and the FALC pro received the reflected signal, performed the mixing, generated the error signal, and tweaked the laser diode’s current to maintain resonance.

Using this setup, we could successfully lock the laser for periods on the order of minutes. Nonetheless, external perturbations easily destabilised it. This was expected as the low-finesse cavity has limited isolation and stability. With the ultrastable cavity, we expect a significant improvement in performance, enabling long-lasting and robust locking.

Additionally, the sidebands introduced by the modulation provide a frequency reference, allowing us to scale the frequency axis of the transmission spectrum. In our case, the sidebands were offset by $\Omega = 25$ MHz from the carrier. This frequency reference enabled us to determine the FWHM and the FSR of the monitoring cavity, from which we calculated the finesse. We obtained $\mathcal{F} = 295 \pm 18$, consistent with the expected $\mathcal{F} \approx 313$.

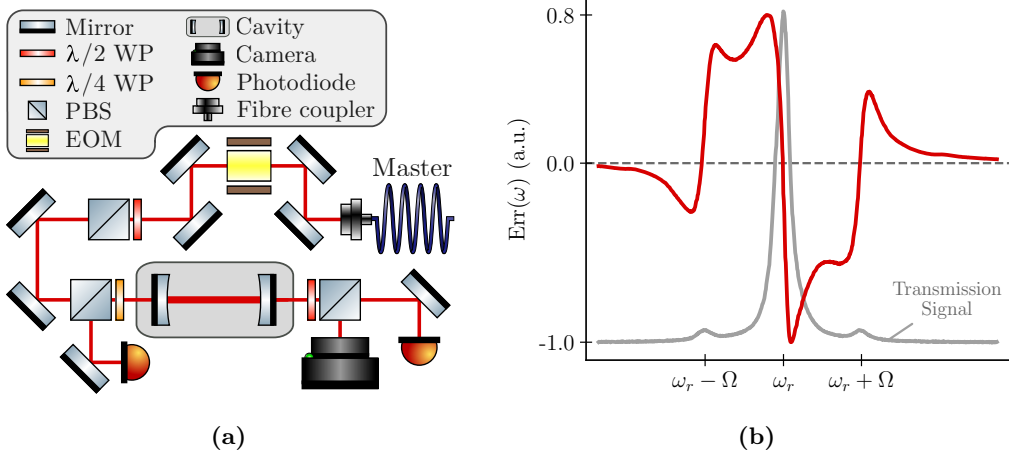


Figure 10: (a) The modified setup for monitoring allows modulating light with an EOM and detecting the reflection from the cavity. (b) With the PDH technique, we measure an error signal that changes sign across resonance frequencies.

⁶TOPTICA, DLC pro + PDH DLC pro Module.

⁷TOPTICA, FALC pro.

3.4 Conclusions and Outlook

In summary, this section has detailed the experimental progress achieved. The work focused primarily on the development of the 689 nm laser system: building the main optical paths, assembling and aligning the slave diode to increase power for the 3D MOT, and setting up the low-finesse cavity to monitor the injection lock. Moreover, we began preparing the ultrastable cavity for laser frequency stabilisation by characterising its finesse and testing the PDH locking technique on the monitoring cavity.

The following steps for the red laser system will focus on integrating the ultrastable cavity. This involves mounting it on a vibration-isolation platform, building the paths for locking the three lasers, and enclosing the setup within an acoustically isolated box.

Beyond laser frequency locking, several components must be completed, including the optical paths to the atoms for the red 3D MOT, Sisyphus cooling and clock excitation. In addition, the 698 nm and Ry excitation laser systems remain to be installed.

4 Conclusions

In this master’s thesis, as outlined in [Sections 2.4](#) and [3.4](#), we have contributed to both the theoretical and practical development of the new Rydberg atom-array experiment at ICFO. The theoretical work clarified the clock excitation scheme, characterised key properties of strontium’s Rydberg states, established boundaries for valid lattice geometries, and demonstrated that selective Rydberg excitation by scaling the optical tweezer’s intensity is feasible. Experimentally, we achieved significant progress on the 689 nm laser system, including the setup of a slave diode for power amplification, characterisation of both low-finesse and ultrastable cavities, and testing of the Pound-Drever-Hall locking technique.

Relative to the overall status of the experiment, beyond what we already presented in [Section 3.4](#) for the red laser system, ongoing efforts focus on building the optics to realise the 3D MOTs and assembling the glass cell with integrated electrodes. These electrodes will enable compensation of stray electric fields, motivating the extension of Rydberg interaction calculations to include such effects and assess the required tolerance levels. Once the glass cell and 3D MOTs are operational, the remaining steps towards the first measurements of our theoretical results include constructing a high-resolution microscope for imaging and generating the tweezers, integrating the optical tweezer array setup, and implementing the Rydberg excitation path.

Ultimately, the advances we report here represent significant progress towards realising a versatile platform for simulating complex many-body quantum phenomena. Successfully implementing the model proposed by A. Celi *et al.* [[13](#)] in our experiment would mark a key milestone towards the quantum simulation of high-dimensional gauge theories, which involve lattice formulations with plaquette interactions.

Bibliography

- [1] Richard P. Feynman. Simulating physics with computers. *Int. J. Theor. Phys.*, 21:467–488, 1982.
- [2] I. M. Georgescu, S. Ashhab, and F. Nori. Quantum simulation. *Reviews of Modern Physics*, 86(1):153–185, March 2014.
- [3] R. Blatt and C. F. Roos. Quantum simulations with trapped ions. *Nature Physics*, 8:277–284, April 2012.
- [4] A. A. Houck, H. E. Türeci, and J. Koch. On-chip quantum simulation with superconducting circuits. *Nature Physics*, 8:292–299, April 2012.
- [5] A. Aspuru-Guzik and P. Walther. Photonic quantum simulators. *Nature Physics*, 8:285–291, April 2012.
- [6] T. Hensgens, T. Fujita, L. Janssen, X. Li, C. J. Van Diepen, C. Reichl, W. Wegscheider, S. Das Sarma, and L. M. K. Vandersypen. Quantum simulation of a Fermi–Hubbard model using a semiconductor quantum dot array. *Nature*, 548:70–73, August 2017.
- [7] T. Langen, G. Valtolina, D. Wang, and J. Ye. Quantum state manipulation and cooling of ultracold molecules. *Nature Physics*, 20:702–712, May 2024.
- [8] I. Bloch, J. Dalibard, and S. Nascimbène. Quantum simulations with ultracold quantum gases. *Nature Physics*, 8:267–276, April 2012.
- [9] C. Gross and I. Bloch. Quantum simulations with ultracold atoms in optical lattices. *Science*, 357(6355):995–1001, September 2017.
- [10] A. Browaeys and T. Lahaye. Many-body physics with individually controlled Rydberg atoms. *Nature Physics*, 16:132–142, January 2020.
- [11] R. Grimm, M. Weidemüller, and Y. B. Ovchinnikov. Optical dipole traps for neutral atoms. *Advances In Atomic, Molecular, and Optical Physics*, 42:95–170, 2000.
- [12] C. Muldoon, L. Brandt, J. Dong, D. Stuart, E. Brainis, M. Himsforth, and A. Kuhn. Control and manipulation of cold atoms in optical tweezers. *New Journal of Physics*, 14:073051, July 2012.
- [13] A. Celi, B. Vermersch, O. Viyuela, H. Pichler, M. D. Lukin, and P. Zoller. Emerging two-dimensional gauge theories in Rydberg configurable arrays. *Physical Review X*, 10(2):021057, June 2020.
- [14] T. F. Gallagher. Rydberg atoms. *Reports on Progress in Physics*, 51:143–188, February 1988.
- [15] J. Dalibard. *From van der Waals universality to Fano-Feshbach resonances*. Collège de France, 2021.
- [16] S. K. Barik, A. Thakur, Y. Jindal, B. S. Slipa, and S. Roy. Quantum technologies with Rydberg atoms. *Frontiers in Quantum Science and Technology*, 3:1426216, July 2024.
- [17] X. Wu, X. Liang, Y. Tian, F. Yang, C. Chen, Y.-C. Liu, M. K. Tey, and L. You. A concise review of Rydberg atom based quantum computation and quantum simulation. *Chinese Physics B*, 30(2):020305, February 2021.
- [18] C. W. Bauer, Z. Davoudi, A. B. Balantekin, T. Bhattacharya, M. Carena, W. A. de Jong, P. Draper, A. El-Khadra, N. Gemelke, M. Hanada, D. Kharzeev, H. Lamm, Y.-Y. Li, J. Liu, M. Lukin, Y. Meurice, C. Monroe, B. Nachman, G. Pagano, J. Preskill, E. Rinaldi, A. Roggero, D. I. Santiago, M. J. Savage, I. Siddiqi, G. Siopsis, D. Van Zanten, N. Wiebe, Y. Yamauchi, K. Yeter-Aydeniz, and S. Zorzetti. Quantum simulation for high-energy physics. *PRX Quantum*, 4(2):027001, May 2023.
- [19] R. Mills. Gauge fields. *American Journal of Physics*, 57(6):493–507, 1989.

- [20] W. N. Cottingham and D. A. Greenwood. *An introduction to the Standard Model of particle physics*. Cambridge University Press, 2nd edition, 2007.
- [21] A. Lopez and E. Fradkin. Fractional quantum Hall effect and Chern-Simons gauge theories. *Physical Review B*, 44(10):5246–5262, September 1991.
- [22] G. Baskaran and P. W. Anderson. Gauge theory of high-temperature superconductors and strongly correlated Fermi systems. *Physical Review B*, 37(1):580–583, January 1988.
- [23] L. Savary and L. Balents. Quantum spin liquids: A review. *Reports on Progress in Physics*, 80:016502, November 2016.
- [24] D. S. Rokhsar and S. A. Kivelson. Superconductivity and the quantum hard-core dimer gas. *Physical Review Letters*, 61(20):2376–2379, November 1988.
- [25] R. Moessner and S. L. Sondhi. Resonating valence bond liquid physics on the triangular lattice. *Progress of Theoretical Physics Supplement*, 145:37–42, February 2002.
- [26] J. Bergmann. *Simulation of lattice gauge theories with Rydberg atom arrays*. Universitat Autònoma de Barcelona — ICFO - The Institute of Photonic Sciences, October 2023.
- [27] B. J. Bloom, T. L. Nicholson, J. R. Williams, S. L. Campbell, M. Bishof, X. Zhang, W. Zhang, S. L. Bromley, and J. Ye. An optical lattice clock with accuracy and stability at the 10^{-18} level. *Nature*, 506:71–75, January 2014.
- [28] R. Santra, K. V. Christ, and C. H. Greene. Properties of metastable alkaline-earth-metal atoms calculated using an accurate effective core potential. *Physical Review A*, 69(4):042510, April 2004.
- [29] R. W. Boyd. *Nonlinear optics*. Academic Press, 4th edition, 2020.
- [30] S. Stellmer, R. Grimm, and F. Schreck. Production of quantum-degenerate strontium gases. *Physical Review A*, 87(1):013611, January 2013.
- [31] A. Urech, I. H. A. Knottnerus, R. J. C. Spreeuw, and F. Schreck. Narrow-line imaging of single strontium atoms in shallow optical tweezers. *Physical Review Research*, 4(2):023245, June 2022.
- [32] H. Katori, M. Takamoto, V. G. Pal’chikov, and V. D. Ovsianikov. Ultrastable optical clock with neutral atoms in an engineered light shift trap. *Physical Review Letters*, 91(17):173005, October 2003.
- [33] C. Cohen-Tannoudji, J. Dupont-Roc, and G. Grynberg. *Atom-photon interactions: Basic processes and applications*. Wiley-VCH, 1998.
- [34] I. S. Madjarov, J. P. Covey, A. L. Shaw, J. Choi, A. Kale, A. Cooper, H. Pichler, V. Schkolnik, J. R. Williams, and M. Endres. High-fidelity entanglement and detection of alkaline-earth Rydberg atoms. *Nature Physics*, 16:857–861, May 2020.
- [35] J. He, B. Pasquiou, R. G. Escudero, S. Zhou, M. Borkowski, and F. Schreck. Coherent three-photon excitation of the strontium clock transition. *Physical Review Research*, 7(1):L012050, March 2025.
- [36] G. Unnikrishnan, P. Ilzhöfer, A. Scholz, C. Hölzl, A. Götzelmann, R. K. Gupta, J. Zhao, J. Krauter, S. Weber, N. Makki, H. P. Büchler, T. Pfau, and F. Meinert. Coherent control of the fine-structure qubit in a single alkaline-earth atom. *Physical Review Letters*, 132(15):150606, April 2024.
- [37] S. Pucher, V. Klüsener, F. Spriestersbach, J. Geiger, A. Schindewolf, I. Bloch, and S. Blatt. Fine-structure qubit encoded in metastable strontium trapped in an optical lattice. *Physical Review Letters*, 132(15):150605, April 2024.
- [38] I. S. Madjarov. *Entangling, controlling, and detecting individual strontium atoms in optical tweezer arrays*. California Institute of Technology, January 2021.

- [39] A. Taichenachev, V. Yudin, C. Oates, C. Hoyt, Z. Barber, and L. Hollberg. Magnetic field-induced spectroscopy of forbidden optical transitions with application to lattice-based optical atomic clocks. *Physical Review Letters*, 96(8):083001, March 2006.
- [40] I. C. Chang. *Handbook of optics (II)*, chapter 12: Acousto-optic devices and application. McGraw-Hill, 2nd edition, 1995.
- [41] M. J. Seaton. Quantum defect theory. *Reports on Progress in Physics*, 46(2):167–257, February 1983.
- [42] S. Weber, C. Tresp, H. Menke, A. Urvoy, O. Firstenberg, H. P. Büchler, and S. Hofferberth. Tutorial: Calculation of Rydberg interaction potentials. *Journal of Physics B: Atomic, Molecular and Optical Physics*, 50(13):133001, June 2017.
- [43] E.J. Robertson, N. Šibalić, R.M. Potvliege, and M.P.A. Jones. ARC 3.0: An expanded Python toolbox for atomic physics calculations. *Computer Physics Communications*, 261:107814, April 2021.
- [44] J. Dobrzyniecki and M. Tomza. Quantum simulation of the central spin model with a Rydberg atom and polar molecules in optical tweezers. *Physical Review A*, 108(5):052618, November 2023.
- [45] H. J. Metcalf and P. van der Straten. *Laser cooling and trapping*. Springer, 1st edition, 1999.
- [46] H. Labuhn, S. Ravets, D. Barredo, L. Béguin, F. Nogrette, T. Lahaye, and A. Browaeys. Single-atom addressing in microtraps for quantum-state engineering using Rydberg atoms. *Physical Review A*, 90(2):023415, August 2014.
- [47] S. de Léséleuc, S. Weber, V. Lienhard, D. Barredo, H. P. Büchler, T. Lahaye, and A. Browaeys. Accurate mapping of multilevel Rydberg atoms on interacting spin-1/2 particles for the quantum simulation of Ising models. *Physical Review Letters*, 120(11):113602, March 2018.
- [48] I. Prieto-Rodríguez. *A laser system for cooling strontium atoms in a new Rydberg atom-array experiment*. Universitat de Barcelona — ICFO - The Institute of Photonic Sciences, August 2023.
- [49] C. J. Foot. *Atomic physics*. Oxford University Press, 2005.
- [50] G. Richmond. *Double-pass acousto-optic modulator system*. Stony Brook University - Laser Teaching Center, May 2018.
- [51] Z. Liu and R. Slavik. Optical injection locking: From principle to applications. *Journal of Lightwave Technology*, 38(1):43–59, January 2020.
- [52] B. E. A. Slaeh and M. C. Teich. *Fundamentals of photonics*, chapter 6.4: Optical activity and magneto-optics. Wiley, 3rd edition, 2019.
- [53] J. G. Meyer, A. Zablach, K. Kapzems, N. Kovalenko, and O. Pronin. Multipass Faraday rotators and isolators. *Optics Express*, 32(17):29227–29238, July 2024.
- [54] A. E. Siegman. *Lasers*. University Science Books, 1986.
- [55] E. Hecht. *Optics*, chapter 9: Interference. Pearson, 5th edition, 2017.
- [56] R. Scheps. *Introduction to laser diode-pumped solid state lasers*, chapter 2: Basic concepts. SPIE Press, 2002.
- [57] *Fabry-Perot interferometer tutorial*. https://www.thorlabs.com/newgrouppage9.cfm?objectgroup_id=9021 [Accessed: 3rd April 2025].
- [58] J. Höschele. *A strontium quantum-gas microscope*. Universitat Politècnica de Catalunya — ICFO - The Institute of Photonic Sciences, March 2024.
- [59] J. A. Boyd and T. Lahaye. A basic introduction to ultrastable optical cavities for laser stabilization. *American Journal of Physics*, 92:50–58, January 2024.
- [60] S. H. Wissenberg. *Stabilizing diode lasers to an ultrastable reference cavity*. Max-Planck-Institut für Quantenoptik, 2017.

- [61] W. D. Callister and D. G. Rethwisch. *Materials science and engineering: An introduction*, chapter 19: Thermal properties. Wiley, 10th edition, 2018.
- [62] R. W. P. Drever, J. L. Hall, F. V. Kowalski, J. Hough, G. M. Ford, A. J. Munley, and H. Ward. Laser phase and frequency stabilization using an optical resonator. *Applied Physics B*, 31:97–105, June 1983.
- [63] E. D. Black. An introduction to Pound–Drever–Hall laser frequency stabilization. *American Journal of Physics*, 69:79–87, January 2001.
- [64] T. Kawanishi. *Electro-optic modulation for photonic networks*. Springer, 2022.
- [65] D. M. Pozar. *Microwave engineering*, chapter 13: Oscillators and mixers. Wiley, 4th edition, 2012.
- [66] D. M. Pozar. *Microwave engineering*, chapter 8: Microwave filters. Wiley, 4th edition, 2012.
- [67] Energy levels of neutral strontium (Sr I). https://www.physics.nist.gov/PhysRefData/Handbook/Tables/strontiumtable5.htm?utm_source=chatgpt.com [Accessed: 6th March 2025].
- [68] Persistent lines of neutral strontium (Sr I). <https://www.physics.nist.gov/PhysRefData/Handbook/Tables/strontiumtable3.htm> [Accessed: 6th March 2025].
- [69] W. J. Eckner, N. D. Oppong, A. Cao, A. W. Young, W. R. Milner, J. M. Robinson, J. Ye, and A. M. Kaufman. Realizing spin squeezing with Rydberg interactions in an optical clock. *Nature*, 621:734–739, August 2023.
- [70] D. Dreon. *Designing and building an ultracold dysprosium experiment: a new framework for light-spin interaction*. Ecole Normale Supérieure (ENS); PSL Research University, June 2017.
- [71] A. A. Urech. *Single strontium atoms in optical tweezers*. Universiteit van Amsterdam, April 2023.
- [72] R. Mukherjee. *Strong interactions in alkaline-earth Rydberg ensembles*. Technischen Universität Dresden, October 2013.
- [73] D. Jiang, B. Arora, M. S. Safronova, and C. W. Clark. Blackbody-radiation shift in a $^{88}\text{Sr}^+$ ion optical frequency standard. *Journal of Physics B: Atomic, Molecular and Optical Physics*, 42:154020, July 2009.
- [74] J. E. Sansonetti. Wavelengths, transition probabilities, and energy levels for the spectra of strontium ions (Sr II through Sr XXXVIII). *Journal of Physical and Chemical Reference Data*, 41:013102–013102–119, February 2012.
- [75] W. Nagourney. *Quantum electronics for atomic physics*, chapter 3.2: Reflection and transmission at an interface. Oxford University Press, 2010.
- [76] Z. K. Ioannidis, P. M. Radmore, and I. P. Giles. Dynamic response of an all-fiber ring resonator. *Optics Letters*, 13(5):422, May 1988.

Annexes

A Numerical Analysis of the Clock State's Magnetic Response

To study the effect of applying a magnetic field on strontium's clock transition, $5s^2\ ^1S_0 \rightarrow 5s5p\ ^3P_0$, we diagonalised the Hamiltonian describing the Zeeman effect. From the results, we were able to compute the linewidth and the Rabi frequency of the transition as a function of the magnetic field.

A.1 Building and Diagonalising the Zeeman Hamiltonian

A magnetic field broadens the clock transition by introducing admixtures of 3P_1 into the 3P_0 state. Thus, it suffices to consider only the 3P_j manifold, with $j \in \{0, 1, 2\}$. In this subspace, we define the basis as $|l, s, j, m_j\rangle$, where the orbital angular momentum and the spin quantum numbers are $l = 1$ and $s = 1$, and $m_j \in [-j, j]$. Thus, the basis states are:

$$\begin{aligned} ^3P_0 &\rightarrow \{|1, 1, 0, 0\rangle\} \\ ^3P_1 &\rightarrow \{|1, 1, 1, -1\rangle, |1, 1, 1, 0\rangle, |1, 1, 1, 1\rangle\} \\ ^3P_2 &\rightarrow \{|1, 1, 2, -2\rangle, |1, 1, 2, -1\rangle, |1, 1, 2, 0\rangle, |1, 1, 2, 1\rangle, |1, 1, 2, 2\rangle\} \end{aligned} \quad (17)$$

The Zeeman effect describes the splitting and mixing of atomic levels by magnetic fields. Its Hamiltonian is

$$\hat{H}_Z = \mu_B \mathbf{B} \cdot (g_l \hat{\mathbf{L}} + g_s \hat{\mathbf{S}}), \quad (18)$$

where the gyromagnetic ratios are $g_l = 1$ and $g_s \approx 2$, and μ_B is the Bohr magneton. Assuming \mathbf{B} is along the quantization axis, the Hamiltonian reduces to

$$\hat{H}_Z = \mu_B B (g_l m_l + g_s m_s), \quad (19)$$

where m_l and m_s are the magnetic quantum numbers.

However, the basis states above do not have well-defined m_l and m_s values. Therefore, we use the Clebsch-Gordan (CG) coefficients, which we obtain using the `sympy` Python package, to rewrite the states in the $|l, m_l, s, m_s\rangle$ basis:

$$|l, s, j, m_j\rangle = \sum_{m_l, m_s} \text{CG}(l, m_l, s, m_s, j, m_j) |l, m_l, s, m_s\rangle. \quad (20)$$

Once we express the states in the basis with well-defined m_l and m_s , computing the 81 matrix elements (9×9 matrix) of \hat{H}_Z , $\langle l, s, j, m_j | \hat{H}_Z | l', s', j', m'_j \rangle$, is straightforward.

To the resulting matrix, we add the unperturbed energies of the original states, a diagonal matrix of the form

$$\hat{H}_0 = \text{diag}(E_{3P_0}, E_{3P_1}, E_{3P_1}, E_{3P_1}, E_{3P_2}, E_{3P_2}, E_{3P_2}, E_{3P_2}, E_{3P_2}). \quad (21)$$

We fix the origin at the clock state, $E_{3P_0} = 0$, and set the remaining energy differences according to the experimental measurements provided by NIST [67].

Finally, we diagonalise $\hat{H}_0 + \hat{H}_Z$ using the `numpy` implementation for Hermitian matrices. Doing so for different values of the magnetic field yields the spectrum and the energy shifts of each level as a function of the applied field.

A.2 Calculating the Linewidth and the Rabi Frequency

From the spectrum of the 3P_j manifold under a magnetic field, it is straightforward to extract the linewidth and Rabi frequency of the clock transition.

For the linewidth, we consider the eigenstate that most closely resembles the clock state, *i.e.*, the one with a larger component of $|1, 1, 0, 0\rangle$ (in the $|l, s, j, m_j\rangle$ basis). From it, the linewidth is

$$\Gamma = \sum_i |c_i|^2 \Gamma_i, \quad (22)$$

where c_i are the coefficients of the eigenstate in the $|l, s, j, m_j\rangle$ basis and Γ_i are the linewidths of the 3P_j states, as reported by NIST [68]. Note that the transition probabilities, A_{ki} , already correspond to the total linewidths of the 3P_j levels. However, these values are for each 3P_j state as a whole and we must divide them by the degeneracy of each level. Furthermore, to convert the result to Hz, we must also divide by a factor 2π .

The Rabi frequency of a transition, $|i\rangle \leftrightarrow |j\rangle$, is defined as

$$\Omega = -\frac{\langle i | \hat{\mathbf{d}} \cdot \mathbf{E} | j \rangle}{\hbar}, \quad (23)$$

where $\hat{\mathbf{d}}$ is the electric dipole operator and \mathbf{E} is the electric field coupling the states. We write the latter as $\mathbf{E} = E_0 \mathbf{u}$, where \mathbf{u} is a unit vector, and relate it to the intensity of the laser, I :

$$\mathbf{E} = \sqrt{\frac{I}{2\varepsilon_0 c}} \mathbf{u}, \quad (24)$$

where ε_0 is the vacuum permittivity and c is the speed of light. Note that we use the Fourier convention, $\mathbf{E} = E_0 (e^{i\omega t} + \text{c.c.})$.

By substituting eq. (24) into eq. (23) we obtain

$$\Omega = -\sqrt{\frac{I}{2\varepsilon_0 c}} \frac{\langle i | \hat{\mathbf{d}} \cdot \mathbf{u} | j \rangle}{\hbar}. \quad (25)$$

In our case, $|i\rangle$ is the eigenstate closest to the clock state and $|j\rangle$ is the absolute ground state, $5s^2 \ ^1S_0 = |0, 0, 0, 0\rangle$. Since the former is expressed as a superposition of $|l, s, j, m_j\rangle$ states, the Rabi frequency reads

$$\Omega = -\frac{1}{\hbar} \sqrt{\frac{I}{2\varepsilon_0 c}} \sum_{l,s,j,m_j} c_{l,s,j,m_j}^* \langle l, s, j, m_j | \hat{\mathbf{d}} \cdot \mathbf{u} | 0, 0, 0, 0 \rangle. \quad (26)$$

Next, we express \mathbf{u} in the spherical basis,

$$\left\{ \mathbf{e}_1 = (\mathbf{e}_x + i\mathbf{e}_y)/\sqrt{2}, \mathbf{e}_0 = \mathbf{e}_z, \mathbf{e}_{-1} = (\mathbf{e}_x - i\mathbf{e}_y)/\sqrt{2} \right\}, \quad (27)$$

to arrive at

$$\Omega = -\frac{1}{\hbar} \sqrt{\frac{I}{2\varepsilon_0 c}} \sum_{l,s,j,m_j} \sum_{q=-1}^1 c_{l,s,j,m_j}^* u_q \langle l, s, j, m_j | \hat{d}_q | 0, 0, 0, 0 \rangle. \quad (28)$$

The Wigner–Eckart theorem allows us to calculate the matrix element in eq. (28) using a CG coefficient:

$$\langle l, s, j, m_j | \hat{d}_q | 0, 0, 0, 0 \rangle = \text{CG}(0, 0, 1, q, j, m_j) d_{j0}, \quad (29)$$

where the reduced dipole matrix element is computed as

$$d_{j0} = \sqrt{\frac{3\varepsilon_0\hbar}{8\pi^2}\lambda_{j0}^3\Gamma_{j0}}. \quad (30)$$

Again, we extract both the wavelength of the transition from the ground state to the corresponding 3P_j state, λ_{j0} , and the associated linewidth, Γ_{j0} , from NIST [68]. In this case, Γ_{j0} correspond directly to the probability amplitudes reported by NIST.

Therefore, the final expression for the Rabi frequency is

$$\Omega = -\sqrt{\frac{3I}{16\pi^2\hbar c}} \sum_{l,s,j,m_j} \sum_{q=-1}^1 c_{l,s,j,m_j}^* u_q \text{CG}(0, 0, 1, q, j, m_j) \sqrt{\lambda_{j0}^3\Gamma_{j0}}. \quad (31)$$

Once more, to convert the results to Hz, we must divide by a factor 2π . Also, note that, throughout the main text, we assumed π -polarised light, *i.e.*, $u_1 = u_{-1} = 0$ and $u_0 = 1$.

Finally, from perturbation theory [38], we know that $c_{l,s,j,m_j}^* \propto B$ for the states that contribute. Consequently, we can factor out the experimental parameters to write

$$\Omega = \tilde{\Omega} \cdot \sqrt{I} \cdot B, \quad (32)$$

where $\tilde{\Omega}$ has units of $\text{kHz} \cdot \sqrt{\frac{\text{cm}^2}{\text{mW}}} \cdot \frac{1}{\text{T}}$.

B Studying Rydberg-Rydberg Interactions with pairinteraction

A key aspect when analysing Rydberg interactions with the `pairinteraction` Python package is the choice of basis for the system.

The general procedure starts by defining a single-atom Rydberg state, $|\text{Ry}\rangle$. This is done by specifying the quantum numbers n , $l = 0$, $j = 1$ and $m_j = 0$, and the pre-calculated data to use, which we set to `"Sr88_triplet"` as we only consider the triplet manifold. After, we define a single-atom system by choosing a basis and setting any external fields. We choose single-atom basis states with $n \in [n - 2, n + 2]$ and $l \leq 2$, as the relevant contributions to the results will mainly arise from nearby levels. Weber *et al.* elaborate further on the relevance of such choices [42]. For the external fields, we set a magnetic field of 20 G along the z -axis to mimic experimental conditions.

Next, the single-atom system defines the two-atom basis. We further constrain the many-body basis to states close in energy to the level of interest $|\text{Ry}, \text{Ry}\rangle$. We set a maximum absolute energy difference of 10 GHz. Finally, we construct the two-atom system by choosing the interatomic distance and the angle between the interatomic axis and the z -axis, which we choose to be 90° (atoms in the xy -plane as planned in the experiment). For perturbative C_6 calculations, we fix the interatomic distance at 30 μm to avoid state mixing.

To validate our approach, we tested it on the $5s47s\ {}^3S_1$ state. In the literature [69], authors report $C_6 = 9.1\ h \cdot \text{GHz} \cdot \mu\text{m}^6$. By fitting the energy spectrum obtained through the diagonalisation of the interaction, in the region where the $|\text{Ry}, \text{Ry}\rangle$ state remains unmixed with other levels, we obtained a value of $C_6 = 8.05\ h \cdot \text{GHz} \cdot \mu\text{m}^6$. The perturbative calculation yields the same result. Therefore, the deviation is around $\sim 10\%$, which we consider acceptable. Expanding the basis sets further did not significantly alter the results.

C Computing Atomic Polarisabilities

Applying degenerate perturbation theory to the electric dipole interaction operator, $-\hat{\mathbf{d}} \cdot \mathbf{E}$, enables a description of the AC-Stark phenomenon in terms of the atomic polarisability operator: $\hat{V}_{\text{LS}} = -\hat{\alpha}|\mathbf{E}|^2$ [70]. The polarisability operator for a state with total angular momentum j is given by

$$\hat{\alpha} = \left\{ \alpha_s |\mathbf{u}|^2 \hat{\mathbf{1}} - i\alpha_v (\mathbf{u}^* \times \mathbf{u}) \frac{\hat{\mathbf{J}}}{2j} + \alpha_t \frac{3[(\mathbf{u}^* \cdot \hat{\mathbf{J}})(\mathbf{u} \cdot \hat{\mathbf{J}}) + (\mathbf{u} \cdot \hat{\mathbf{J}})(\mathbf{u}^* \cdot \hat{\mathbf{J}})] - 2|\mathbf{u}|^2 \hat{\mathbf{J}}^2}{2j(2j-1)} \right\}, \quad (33)$$

where \mathbf{u} is the complex unit vector indicating the light's polarisation in the spherical basis (see eq. (27)), $\hat{\mathbf{J}} = (\hat{J}_x, \hat{J}_y, \hat{J}_z)$ is the standard total angular momentum operator, and the scalar, vector and tensor polarisabilities are

$$\alpha_s(j) = -\sqrt{\frac{1}{3(2j+1)}} \sum_{j'} (-1)^{j+j'} \begin{Bmatrix} 1 & 0 & 1 \\ j & j' & j \end{Bmatrix} \frac{d_{jj'}^2}{\hbar} \cdot \text{Re} \left(\frac{1}{\omega_{j'j} - \omega - i\Gamma_{j'j}/2} + \frac{1}{\omega_{j'j} + \omega - i\Gamma_{j'j}/2} \right), \quad (34)$$

$$\alpha_v(j) = -\sqrt{\frac{6j}{(j+1)(2j+1)}} \sum_{j'} (-1)^{j+j'} \begin{Bmatrix} 1 & 1 & 1 \\ j & j' & j \end{Bmatrix} \frac{d_{jj'}^2}{\hbar} \cdot \text{Re} \left(\frac{1}{\omega_{j'j} - \omega - i\Gamma_{j'j}/2} - \frac{1}{\omega_{j'j} + \omega - i\Gamma_{j'j}/2} \right), \quad (35)$$

$$\alpha_t(j) = \sqrt{\frac{10j(2j-1)}{3(j+1)(2j+1)(2j+3)}} \sum_{j'} (-1)^{j+j'} \begin{Bmatrix} 1 & 2 & 1 \\ j & j' & j \end{Bmatrix} \frac{d_{jj'}^2}{\hbar} \cdot \text{Re} \left(\frac{1}{\omega_{j'j} - \omega - i\Gamma_{j'j}/2} + \frac{1}{\omega_{j'j} + \omega - i\Gamma_{j'j}/2} \right). \quad (36)$$

We set the laser frequency, ω , to the one of 813 nm light. Recall that reduced dipole matrix elements of the transition $j' \leftrightarrow j$ are related to decay rates and transition frequencies by

$$d_{jj'} = \sqrt{\frac{3\pi\epsilon_0 \hbar c^3}{\omega_{jj'}^3} \Gamma_{jj'}}. \quad (37)$$

To compute the polarisability of the clock state, we extracted the reduced dipole matrix elements and the transition frequencies from [71, Table 3.3]. Assuming the Fourier convention, $\mathbf{E} = E_0 (e^{i\omega t} + \text{c.c.})$, we use $I = 2\epsilon_0 c |E|^2$ to write $\hat{V}_{\text{LS}} = -\frac{\hat{\alpha}}{2\epsilon_0 c} I$.

Furthermore, we include a correction to the scalar polarisability to account for non-dominant transitions and core effects, $\alpha_s \rightarrow \alpha_s + \alpha_{\text{core}}$, modelled using empirical parameters as described in [71, Section 3.1.1]:

$$\alpha_{\text{core}} = a + \frac{b}{\lambda - c}. \quad (38)$$

C.1 Atomic Polarisabilities of Rydberg States

Experimental data for Rydberg states is not readily available to compute atomic polarisabilities using the procedure described above. Instead, we follow the method presented by R. Mukherjee [72], consisting of separating the polarisability of the Rydberg electron and the one from the inner electrons, *i.e.*, from the Sr^+ ionic core.

We compute the contribution from the ionic core, α_{nucleus} , using the same method described above with the data for the transitions of Sr^+ , extracted from [73, 74]. Note that, since $j = 1/2$ for the ionic core, the tensor polarisability vanishes (see eq. (36)).

The Rydberg electron polarisability, α_{Ry} , can be computed by assuming that the electron is quasi-free. In this regime, the potential it experiences due to the oscillating electric field at ω , known as the ponderomotive potential, is given by

$$V = \frac{e^2 |\mathbf{E}|^2}{m_e \omega}, \quad (39)$$

where e and m_e are the electron's charge and mass, respectively.

Comparing eq. (39) to the expression for the light shift operator, $\hat{V}_{\text{LS}} = -\hat{\alpha} |\mathbf{E}|^2$, we see that the effective polarisability of the Rydberg electron is

$$\alpha_{\text{Ry}} = -\frac{e^2}{m_e \omega}. \quad (40)$$

Note that this expression differs from the one in [72], as they use the complex convention, where the field is $\mathbf{E} = \text{Re}(\mathcal{E} e^{i\omega t})$, instead of the Fourier convention that we use.

Finally, we obtain the total polarisability for a Rydberg atom as

$$\alpha_{\text{tot}} = \alpha_{\text{nucleus}} + \alpha_{\text{Ry}}. \quad (41)$$

D Reflection Signal of an Optical Cavity when Scanning the Frequency

When the frequency of light coupled to an optical cavity is scanned, the reflection signal exhibits chirped oscillations that decay exponentially [59]. To understand this observation, we derive an analytical expression for the reflected field here. First, with a time-dependent laser frequency, $\omega(t)$, the electric field⁸ incident to the cavity is

$$E_{\text{inc}}(t) = \mathcal{E} e^{i\varphi(t)}, \quad (42)$$

where the phase is given by

$$\varphi(t) = \int_{-\infty}^t \omega(t') dt'. \quad (43)$$

The light that reflects from the cavity is a superposition of two fields:

$$E_{\text{refl}}(t) = \sqrt{R} \cdot E_{\text{inc}}(t) + \sum_{n=1}^{\infty} T R^{n-1/2} \cdot E_n(t). \quad (44)$$

The first term represents the portion of light reflected directly at the input mirror without entering the cavity. Since we are working with electric fields, its amplitude is proportional to \sqrt{R} , where R is the intensity reflection coefficient of the mirrors. This component acquires no additional phase, as it reflects off the back surface of the mirror [75].

⁸Note we adopt the complex convention and omit the polarisation, which does not affect this derivation.

The second contribution accounts for the field that couples into the cavity and leaks back out through the input mirror. Each term in the sum corresponds to a wavefront that has undergone n round trips inside the cavity before exiting. This light must transmit twice through the input mirror (entry and exit), yielding a factor of $\sqrt{T} \cdot \sqrt{T}$ in amplitude. After n round trips, the wave has reflected $2n - 1$ times, leading to $(\sqrt{R})^{2n-1}$. Therefore, the total amplitude associated with the n -th round trip is proportional to $TR^{n-1/2}$. The corresponding field is

$$E_n(t) = \mathcal{E} e^{i\varphi(t-\theta n)} e^{i\pi}, \quad (45)$$

where $\theta = 2L/c$ is the round trip time, defined by the cavity's length and the speed of light. This expression captures the phase evolution of a wavefront that entered the cavity $\Delta t = \theta n$ earlier, so it exits after n round trips. The additional π phase accounts for the odd number of front-surface reflections.

Now, we can introduce the relation between the intensity reflection and transmission coefficients, $R + T = 1$, the fact that $e^{i\pi} = -1$, factor out the incident field, and define a new index $m = n - 1$ to get

$$E_{\text{refl}}(t) = \sqrt{R} \cdot \mathcal{E} e^{i\varphi(t)} \left[1 - (1 - R) \sum_{m=0}^{\infty} R^m e^{i\varphi_m(t)} \right], \quad (46)$$

where we have defined

$$\varphi_m(t) := \varphi[t - \theta(m + 1)] - \varphi(t) = - \int_{t-\theta(m+1)}^t \omega(t') dt'. \quad (47)$$

Assuming that the frequency is scanned linearly, $\omega(t) = \omega_0 + \alpha t$, we get

$$\varphi_m(t) = \frac{\alpha}{2}(m + 1)^2\theta^2 - (\omega_0 + \alpha t)(m + 1)\theta \quad (48)$$

For a high finesse cavity, $R \approx 1$, so R^m does not vary significantly between different m . If the phase $\varphi_m(t)$ also varied slowly, we could approximate the summation in [eq. \(46\)](#) by an integral. Thus, we compute

$$\frac{d\varphi_m(t)}{dm} \Delta m = \alpha(m + 1)\theta^2 - (\omega_0 + \alpha t)\theta, \quad (49)$$

where we used $\Delta m = 1$. Assuming that the scan rate is small ($\omega_0 \gg \alpha t$) and that ω_0 is a resonance, as it is an arbitrary choice:

$$\frac{d\varphi_m(t)}{dm} \Delta m \approx \alpha(m + 1)\theta^2 - 2\pi p, \quad (50)$$

where we have introduced the resonance condition ([eq. \(10\)](#)) with $p \in \mathbb{Z}$. Lastly, due to the finite dimensions of the cavity, we can take $\alpha\theta^2 = \alpha \frac{4L^2}{c^2} \ll c$. Since terms in the sum with significantly large m will be suppressed by the decay of R^m (because $R < 1$), we have

$$\frac{d\varphi_m(t)}{dm} \Delta m \approx -2\pi p, \quad (51)$$

which implies a slowly varying phase between m values and makes it valid to replace the summation with an integral:

$$E_{\text{refl}}(t) = \sqrt{R} \cdot \mathcal{E} e^{i\varphi(t)} \left[1 - (1 - R) \int_0^{\infty} R^m e^{i\varphi_m(t)} dm \right]. \quad (52)$$

Focusing on the second term of eq. (52) and expanding $\varphi_m(t)$ we get

$$\mathcal{I} := (1 - R)e^{i[\frac{\alpha}{2}\theta^2 - (\omega_0 + \alpha t)\theta]} \int_0^\infty R^m e^{i\{\frac{\alpha}{2}\theta^2 m^2 + [\alpha\theta^2 - (\omega_0 + \alpha t)\theta]m\}} dm. \quad (53)$$

Introducing $R^m = e^{m \ln(R)}$:

$$\mathcal{I} := (1 - R)e^{i[\frac{\alpha}{2}\theta^2 - (\omega_0 + \alpha t)\theta]} \int_0^\infty e^{i\{\frac{\alpha}{2}\theta^2 m^2 + [\alpha\theta^2 - (\omega_0 + \alpha t)\theta - i \ln(R)]m\}} dm, \quad (54)$$

which we ultimately rewrite as

$$\mathcal{I} := (1 - R)e^{i[\frac{\alpha}{2}\theta^2 - (\omega_0 + \alpha t)\theta]} \int_0^\infty e^{-im^2 \tilde{\alpha} \tilde{\theta} / 2 - \lambda m} dm, \quad (55)$$

where we defined $\tilde{\alpha} := -\alpha$, $\tilde{\theta} := \theta^2$ and $\lambda := -i[\alpha\theta^2 - (\omega_0 + \alpha t)\theta] - \ln(R)$. The result of this integral is provided by Z. K. Ioannidis *et al.* [76], and yields:

$$\mathcal{I} := (1 - R)e^{i[\frac{\alpha}{2}\theta^2 - (\omega_0 + \alpha t)\theta]} \sqrt{\frac{\pi}{2i\tilde{\alpha}\tilde{\theta}}} e^{-i\frac{\lambda^2}{2\tilde{\alpha}\tilde{\theta}}} \left[1 - \operatorname{erf}\left(\frac{\lambda}{\sqrt{2i\tilde{\alpha}\tilde{\theta}}}\right) \right], \quad (56)$$

where $\operatorname{erf}(x)$ is the error function.

Since the intensity is proportional to the squared amplitude of the field, one can plot $I(t) \propto E_{\text{refl}}(t)E_{\text{refl}}^*(t)$ by inserting the result in eq. (56) to obtain the chirped oscillations with exponential decay. However, we further show analytically how the exponential in eq. (56) results in the decay that allows us to characterise the finesse of the cavity.

The exponential decay comes from the imaginary part in λ^2 ,

$$\operatorname{Im}(\lambda^2) = 2 \ln(R) [\alpha\theta^2 - (\omega_0 + \alpha t)\theta], \quad (57)$$

and only the time dependence is relevant to us:

$$e^{-i\frac{-2i \ln(R)\alpha\theta}{2\tilde{\alpha}\tilde{\theta}}t} = e^{\frac{\ln(R)}{\theta}t}. \quad (58)$$

We rewrite $\ln(R) = \ln[1 - (1 - R)]$ and, since $1 - R \approx 0$ for high-finesse cavities, we Taylor expand

$$\ln(R) = \ln[1 - (1 - R)] \approx -(1 - R), \quad (59)$$

yielding

$$e^{\frac{\ln(R)}{\theta}t} = e^{-\frac{t}{\theta/(1-R)}}. \quad (60)$$

This expression evinces the exponential decay of the reflection signal and defines the cavity decay time, τ , found in the main text:

$$\tau := \frac{\theta}{1 - R} = \frac{2L}{c(1 - R)} = \frac{1}{\Delta\nu_{\text{FSR}}(1 - R)}. \quad (61)$$

E Pictures of the Experimental Setup

In the next pages we include pictures of the experimental setup in chronological order.

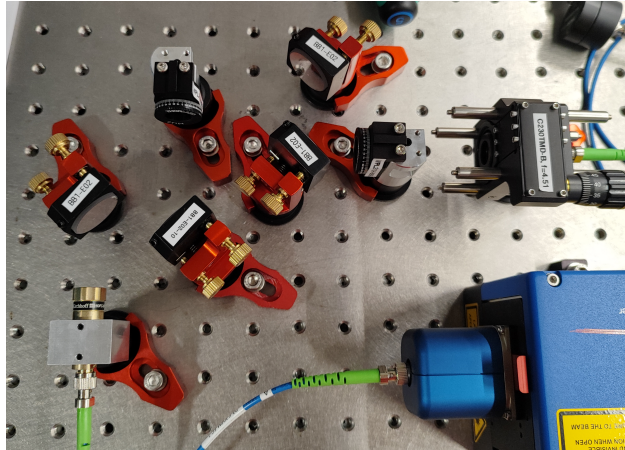


Figure 11: 21/01/2021 - First steps in the main paths.

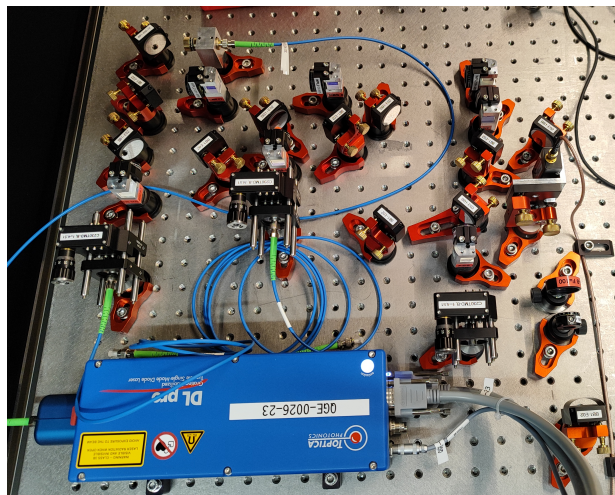


Figure 12: 25/02/2025 - Completion of the master monitoring, 3D MOT and Sisyphus cooling main paths.



Figure 13: 03/03/2025 - Addition of the ultrastable cavity main path.

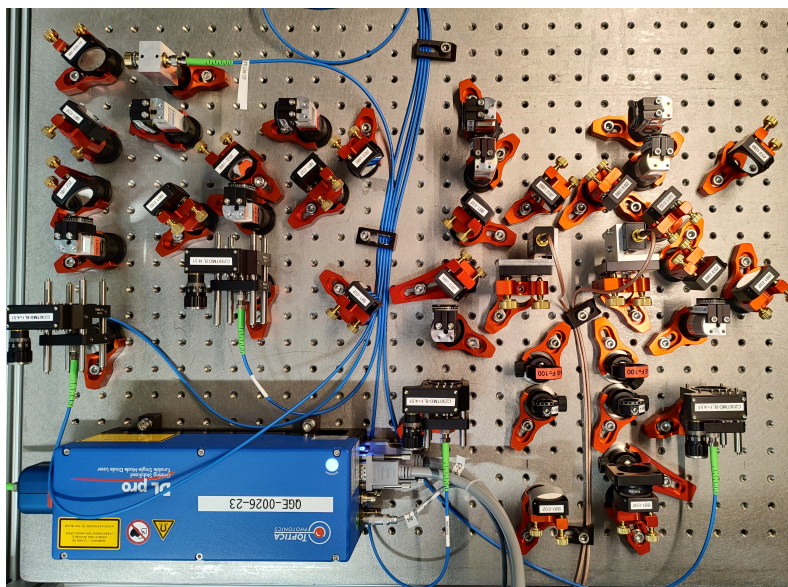


Figure 14: 06/03/2025 - Restructuring of the ultrastable cavity main path.

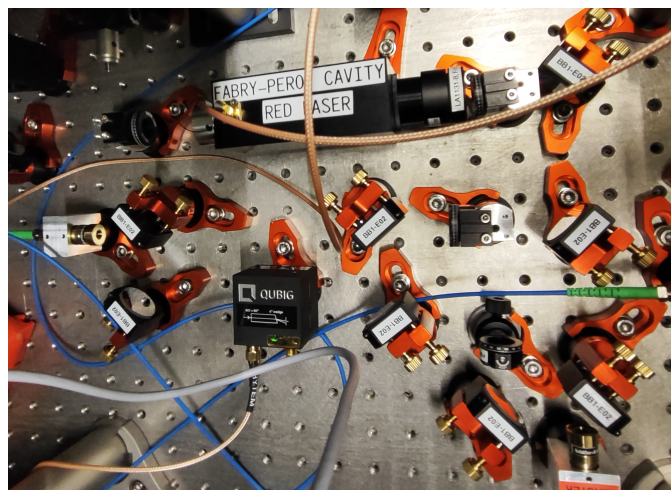


Figure 15: 13/03/2025 - Completion of the monitoring setup.

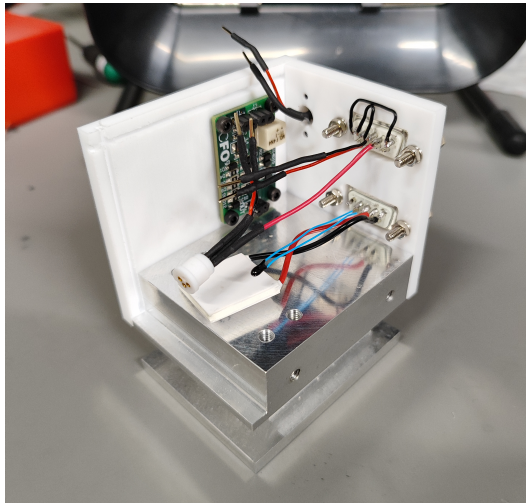


Figure 16: 11/04/2025 - Assembly of the slave diode (I).

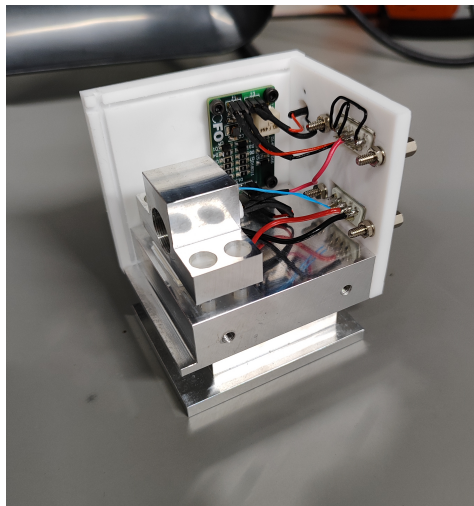


Figure 17: 11/04/2025 - Assembly of the slave diode (II).

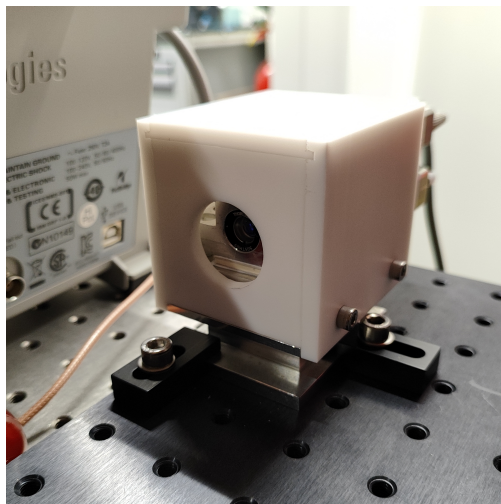


Figure 18: 11/04/2025 - Assembly of the slave diode (III).



Figure 19: 08/05/2025 - Completion of the slave diode setup.

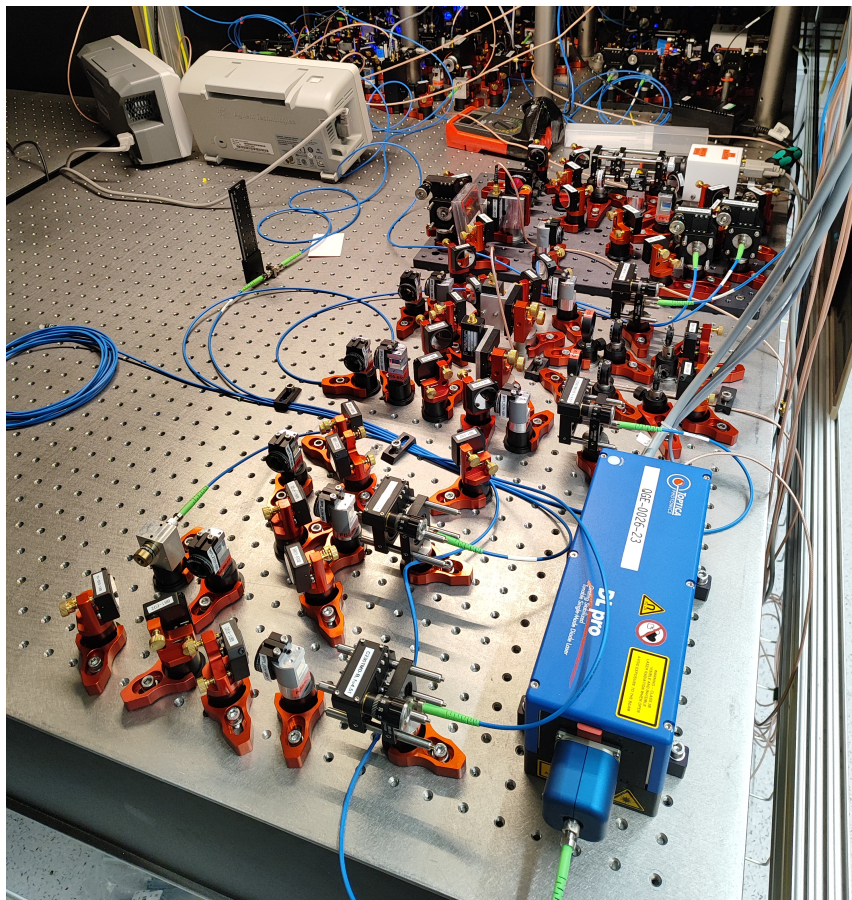


Figure 20: 08/05/2025 - Overview of the main paths (front) and the slave diode setup (back).

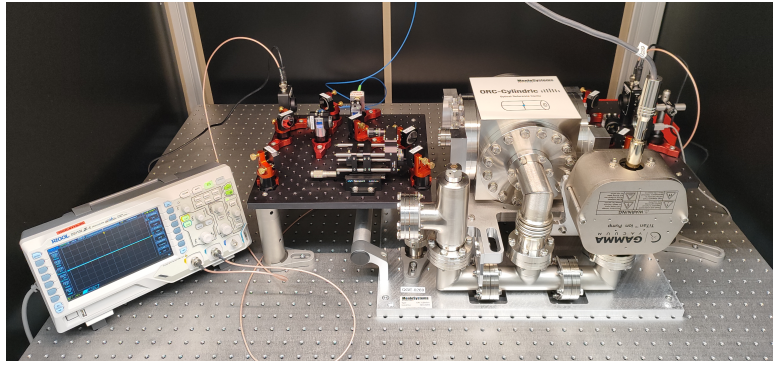


Figure 21: 06/06/2025 - Completion of the temporary characterisation setup (overview).

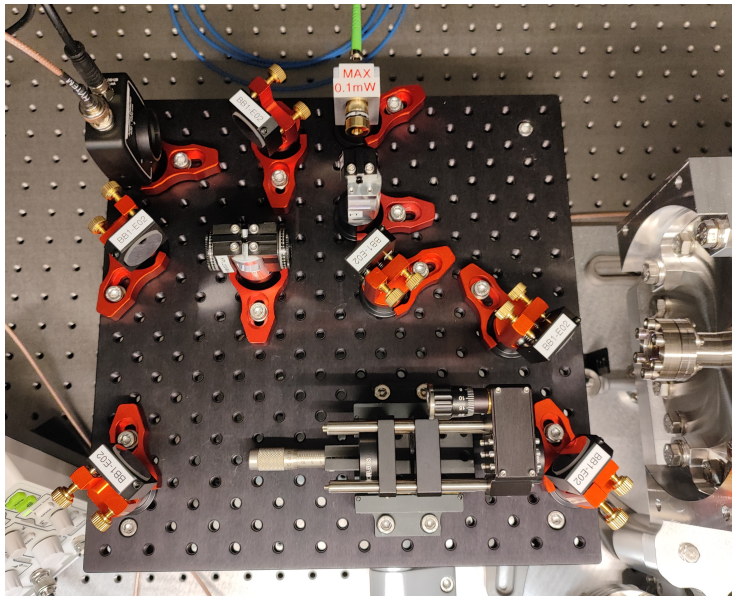


Figure 22: Completion of the temporary characterisation setup (reflection).

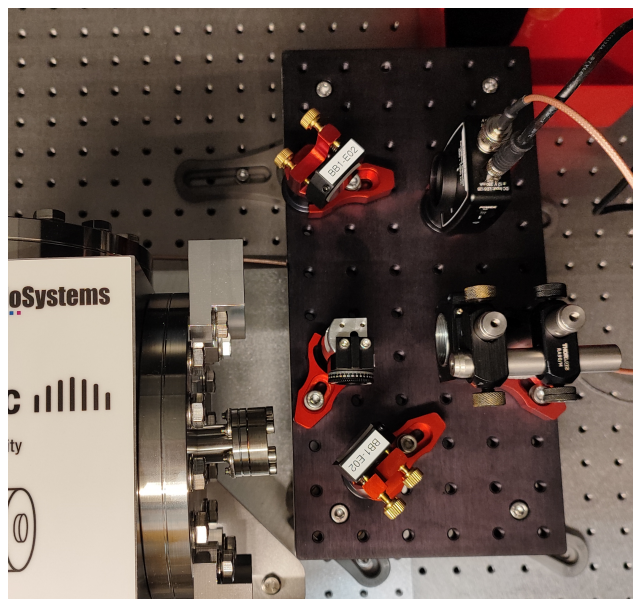


Figure 23: Completion of the temporary characterisation setup (transmission).